Exploring the directly imaged HD 1160 system through spectroscopic characterization and high-cadence variability monitoring

Ben J. Sutlieff [1,2,3,4]★ Jayne L. Birkby [5] Jordan M. Stone [6] Annelotte Derkink,[3] Frank Backs [3,7]
David S. Doelman,[4,8] Matthew A. Kenworthy [4] Alexander J. Bohn [4] Steve Ertel,[9,10] Frans Snik,[4]
Charles E. Woodward,[11] Ilya Ilyin,[12] Andrew J. Skemer,[13] Jarron M. Leisenring [9]
Klaus G. Strassmeier,[12] Ji Wang (王吉),[14] David Charbonneau[15] and Beth A. Biller[1,2]

[1]*Scottish Universities Physics Alliance, Institute for Astronomy, University of Edinburgh, Royal Observatory, Blackford Hill, Edinburgh EH9 3HJ, UK*
[2]*Centre for Exoplanet Science, University of Edinburgh, Edinburgh EH9 3HJ, UK*
[3]*Anton Pannekoek Institute for Astronomy, University of Amsterdam, Science Park 904, NL-1098 XH Amsterdam, the Netherlands*
[4]*Leiden Observatory, Leiden University, PO Box 9513, NL-2300 RA Leiden, the Netherlands*
[5]*Astrophysics, University of Oxford, Denys Wilkinson Building, Keble Road, Oxford OX1 3RH, UK*
[6]*Naval Research Laboratory, Remote Sensing Division, 4555 Overlook Ave. SW, Washington, DC 20375, USA*
[7]*Institute of Astrophysics, Universiteit Leuven, Celestijnenlaan 200 D, B-3001 Leuven, Belgium*
[8]*SRON Netherlands Institute for Space Research, Niels Bohrweg 4, NL-2333 CA Leiden, the Netherlands*
[9]*Department of Astronomy and Steward Observatory, University of Arizona, 933 N. Cherry Ave., Tucson, AZ 85721, USA*
[10]*Large Binocular Telescope Observatory, University of Arizona, 933 North Cherry Avenue, Tucson, AZ 85721, USA*
[11]*Minnesota Institute for Astrophysics, University of Minnesota, 116 Church Street SE, Minneapolis, MN 55455, USA*
[12]*Leibniz-Institute for Astrophysics Potsdam (AIP), An der Sternwarte 16, D-14482 Potsdam, Germany*
[13]*Department of Astronomy and Astrophysics, University of California, Santa Cruz, 1156 High St, Santa Cruz, CA 95064, USA*
[14]*Department of Astronomy, The Ohio State University, 140 W. 18th Ave., Columbus, OH 43210, USA*
[15]*Center for Astrophysics | Harvard & Smithsonian, 60 Garden Street, Cambridge, MA 02138, USA*

ABSTRACT

The time variability and spectra of directly imaged companions provide insight into their physical properties and atmospheric dynamics. We present follow-up $R \sim 40$ spectrophotometric monitoring of red companion HD 1160 B at 2.8–4.2 µm using the double-grating 360° vector Apodizing Phase Plate (dgvAPP360) coronagraph and ALES integral field spectrograph on the Large Binocular Telescope Interferometer. We use the recently developed technique of gvAPP-enabled differential spectrophotometry to produce differential light curves for HD 1160 B. We reproduce the previously reported ∼3.2 h periodic variability in archival data, but detect no periodic variability in new observations taken the following night with a similar 3.5 per cent level precision, suggesting rapid evolution in the variability of HD 1160 B. We also extract complementary spectra of HD 1160 B for each night. The two are mostly consistent, but the companion appears fainter on the second night between 3.0–3.2 µm. Fitting models to these spectra produces different values for physical properties depending on the night considered. We find an effective temperature $T_{\rm eff}$ = 2794^{+115}_{-133} K on the first night, consistent with the literature, but a cooler $T_{\rm eff}$ = 2279^{+79}_{-157} K on the next. We estimate the mass of HD 1160 B to be 16–81 $M_{\rm Jup}$, depending on its age. We also present $R = 50\,000$ high-resolution optical spectroscopy of host star HD 1160 A obtained simultaneously with the PEPSI spectrograph. We reclassify its spectral type to A1 IV-V and measure its projected rotational velocity $v \sin i = 96^{+6}_{-4}$ km s^{-1}. We thus highlight that gvAPP-enabled differential spectrophotometry can achieve repeatable few per cent level precision and does not yet reach a systematic noise floor, suggesting greater precision is achievable with additional data or advanced detrending techniques.

Key words: instrumentation: high angular resolution – planets and satellites: atmospheres – planets and satellites: detection – brown dwarfs – stars: individual: HD 1160 – infrared: planetary systems.

1 INTRODUCTION

With the aid of the latest advancements in adaptive optics and coronagraphic instrumentation, the technique of direct high-contrast

imaging has uncovered ∼30 planetary-mass companions in wide orbits around their host stars (e.g. Marois et al. 2010; Bailey et al. 2014a; Bowler et al. 2017; Keppler et al. 2018; Haffert et al. 2019; Bohn et al. 2020a,b, 2021; Currie et al. 2022, 2023; Hinkley et al. 2023). Furthermore, searches for such objects have also identified a population of higher mass substellar companions up to the brown dwarf/stellar boundary (e.g. Biller et al. 2010; Mawet et al. 2015;

★ E-mail: ben.sutlieff@roe.ac.uk

Konopacky et al. 2016; Milli et al. 2017; Rickman et al. 2020, 2024; Bonavita et al. 2022; Kuzuhara et al. 2022; Franson et al. 2023; Li et al. 2023). These brown dwarf companions are generally brighter than exoplanets and hence easier to observe, yet often appear to have similar properties to giant exoplanets, sharing similar effective temperatures, surface gravities, and weather (e.g. Dupuy & Kraus 2013; Faherty et al. 2013, 2016; Helling & Casewell 2014; Skemer et al. 2016; Morley et al. 2018; Vos et al. 2019; Ashraf et al. 2022; Liu et al. 2024). Studies of brown dwarfs as exoplanet analogues may therefore also help us to understand the underlying processes in exoplanet atmospheres and to break degeneracies surrounding formation mechanisms, which may differ between the two populations despite their similarities.

While spectroscopic observations allow us to derive values for the physical parameters of brown dwarfs through comparisons of companion spectra to atmospheric models, high-cadence variability monitoring provides insight into the dynamics and structure of atmospheric features such as clouds and storms (e.g. Kostov & Apai 2013; Crossfield et al. 2014; Karalidi et al. 2016; Manjavacas et al. 2019, 2021, 2022, 2023; Vos et al. 2022, 2023; Hood et al. 2024; Lew et al. 2024). Variability has now been detected in the light curves of numerous planetary-mass and brown dwarf companions using observations obtained with space-based telescopes (e.g. Zhou et al. 2016, 2020, 2022; Miles-Páez et al. 2019; Bowler et al. 2020b; Lew et al. 2020; Miles-Páez 2021). However, obtaining similar measurements using ground-based telescopes, which have the large diameters needed to resolve companions at close angular separations, has proven more challenging. Non-astrophysical variability induced by turbulence in Earth's atmosphere overwhelms any variability signal from the atmosphere of a faint companion. While the companion's host star would be an ideal photometric reference with which to divide out these systematics and recover its intrinsic variability, this is often obscured by the focal-plane coronagraphs used by most coronagraphic imagers (e.g. Ruane et al. 2018). Nonetheless, ground-based variability studies with coronagraphic imagers have been shown to be possible using satellite spots as photometric references for the companion light curve, with which upper limits for variability have been found for the exoplanets orbiting HR 8799 (Wang et al. 2014, 2022; Jovanovic et al. 2015b; Apai et al. 2016; Biller et al. 2021).

Another, more recently developed approach for exploring the variability of high-contrast companions from the ground involves using the technique of differential spectrophotometry in combination with a vector Apodizing Phase Plate (vAPP) coronagraph (Sutlieff et al. 2023). vAPP coronagraphs offer a breakthrough in high-contrast variability searches as they provide a reliable photometric reference as a result of their intrinsic design; unlike focal-plane coronagraphs, they enable observations of high-contrast companions at close separations while maintaining a Point Spread Function (PSF) of the target star that can be used as a simultaneous photometric reference (Snik et al. 2012; Otten et al. 2014; Doelman et al. 2021; Sutlieff et al. 2021; Liu et al. 2023). To obtain differential spectrophotometry, a vAPP can be combined with an integral field spectrograph (IFS) to spectrally disperse the light from the target. The spectra can then be recombined into white-light, reducing the impact of systematic errors in any single wavelength channel and therefore producing light curves with higher precision (Sutlieff et al. 2023). The light curve of the companion is then divided by the light curve of the photometric reference (in this case the host star) to remove systematic variability trends shared by both objects. This concept of differential spectrophotometry was also used for the satellite spot study of Wang et al. (2022), and is commonplace in the

field of exoplanet transmission spectroscopy (e.g. Diamond-Lowe et al. 2018, 2020a, 2023; Todorov et al. 2019; Arcangeli et al. 2021; Panwar et al. 2022a,b). To demonstrate this technique, Sutlieff et al. (2023) observed HD 1160 B, a companion with a peculiar spectrum at the brown dwarf/stellar boundary, for one night with the double-grating $360°$ vector Apodizing Phase Plate (dgvAPP360; Doelman et al. 2017, 2020, 2021) coronagraph combined with the Arizona Lenslets for Exoplanet Spectroscopy (ALES) IFS on the Large Binocular Telescope. They detected significant sinusoidal variability in the differential white-light curve of this companion with a semi-amplitude of 8.8 per cent and a period of ∼3.24 h. Furthermore, they obtained a 3.7 per cent precision in bins of 18 min, after a multiple linear regression approach was applied to the differential white-light curve to remove residual systematics arising from non-astrophysical sources such as airmass and detector position. This study found no evidence of having reached a systematic noise floor in their single epoch of observations, indicating that the data were not systematic-limited and that additional data could further improve the sensitivity to variability.

In this work, we further monitor and characterize HD 1160 B and its host star HD 1160 A using additional observations obtained with the Large Binocular Telescope (LBT). This includes a further night of variability monitoring of HD 1160 B with ALES + dg-vAPP360, which we also use to produce its complementary spectral characterization using the 2.8–4.2 µm spectra from both epochs. We separately characterize the host star HD 1160 A using data obtained simultaneously with the PEPSI high resolution spectrograph. The differential spectrophotometry observations with ALES + dgvAPP360 also allow us to test the repeatability of the light curve precision achieved by Sutlieff et al. (2023) in their pilot study. In Section 2, we review the properties of the HD 1160 system. Our observations of this system are then described in Section 3, and in Section 4 we describe the methods used to reduce the data from each instrument and extract photometry of the targets. In Section 5, we investigate the variability of HD 1160 B by using the ALES + dgvAPP360 data to produce differential spectrophotometric light curves. We also use these data in Section 6 to produce and study the spectrum of HD 1160 B. The data obtained with PEPSI are analysed in Section 7, in which we explore the spectrum of HD 1160 A. The results found in each of these three sections are then discussed in Section 8. Finally, we summarize the conclusions of the paper in Section 9.

2 TARGET PROPERTIES

The HD 1160 system is located at a distance of 120.7 ± 0.5 pc (Gaia Data Release 3; Gaia Collaboration 2016, 2023). In Table 1, we summarize literature values for key properties of the stellar primary component HD 1160 A, for which Houk & Swift (1999) assigned a spectral type of A0 V using photographic plates on the 0.61-m Curtis Schmidt telescope at the Cerro Tololo Inter-American Observatory (CTIO). Using observations from the *Transiting Exoplanet Survey Satellite* (*TESS*) mission, Sutlieff et al. (2023) found that HD 1160 A is non-variable in the optical at the 0.03 per cent level, and *Spitzer* observations by Su et al. (2006) found no infrared excess, suggesting that there is not significant warm circumstellar dust present. Nielsen et al. (2012) identified two comoving companions to HD 1160 A at separations of ∼80 au (∼0.78 arcsec) and ∼530 au (∼5.15 arcsec), known as HD 1160 B and C, respectively, during the Gemini Near-Infrared Coronagraphic Imager (NICI) Planet-Finding Campaign (Liu et al. 2010). HD 1160 B has a contrast of $\Delta L' = 6.35 \pm 0.12$ mag relative to the $L' = 7.055 \pm 0.014$ mag of

Table 1. Properties of host star HD 1160 A.

Property	Value	Ref.
Right Ascension (J2000, hh:mm:ss.ss)	00:15:57.32	(1)
Declination (J2000, dd:mm:ss.ss)	+04:15:03.77	(1)
RA proper motion (mas yr^{-1})	20.150 ± 0.040	(1)
Dec. proper motion (mas yr^{-1})	-14.903 ± 0.034	(1)
Parallax (mas)	8.2721 ± 0.0355	(1)
Radial velocity (km s^{-1})	13.5 ± 0.5	(1)
Distance (pc)	120.7 ± 0.5	(1)
Extinction A_V (mag)	0.16	(1)
Spectral type	A0 V	(2)
	A1 IV-V	(3)
Mass (M$_\odot$)	~ 2.2	(4)
$T_{\rm eff}$ (K)	9011 ± 85	(5)
	9200^{+200}_{-100}	(3)
log(g) (dex)	~ 4.5	(6)
	$3.5^{+0.5}_{-0.3}$	(3)
$v \sin i$ (km s^{-1})	96^{+6}_{-4}	(3)
log(L/L$_\odot$)	1.12 ± 0.07	(5)
[Fe/H]	$\sim$solar	(6)
V (mag)	7.119 ± 0.010	(7)
Gaia G (mag)	7.1248 ± 0.0004	(1)
J (mag)	6.983 ± 0.020	(8)
H (mag)	7.013 ± 0.023	(8)
K (mag)	7.040 ± 0.029	(8)
L$'$ (mag)	7.055 ± 0.014	(9)
M$'$ (mag)	7.04 ± 0.02	(9)
System age (Myr)	50^{+50}_{-40}	(4)
	100^{+200}_{-70}	(10)
	20–125	(5)
	~ 120	(11)
	10–20	(6)

Note. References: (1) Gaia Collaboration (2016, 2023), (2) Houk & Swift (1999), (3) This work; (4) Nielsen et al. (2012), (5) Garcia et al. (2017), (6) Mesa et al. (2020), (7) Tycho-2 (Høg et al. 2000a,b), (8) 2MASS (Cutri et al. 2003; Skrutskie et al. 2006), (9) Leggett et al. (2003), (10) Maire et al. (2016), (11) Curtis et al. (2019).

HD 1160 A, and its orbit is almost edge-on, with an inclination angle of $92^{+8.7}_{-9.3}{}^\circ$ (Leggett et al. 2003; Nielsen et al. 2012; Bowler, Blunt & Nielsen 2020a). The wide angular separation of HD 1160 C places it beyond the fields of view of the data sets in this paper.

Nielsen et al. (2012) found HD 1160 B to be an L0 $\pm$ 2 brown dwarf based on their near-infrared photometry, and that their near-infrared spectrum of HD 1160 C best matches that of an M3.5 $\pm$ 0.5 low-mass star. They found that both companions are redder than similar objects, which combined with an apparent underluminosity of HD 1160 A suggests a young age of 50^{+50}_{-40} Myr. Combining this age range with the luminosity of HD 1160 B, they derived a value for its mass of 33^{+12}_{-9} $M_{\rm Jup}$.

However, using observations from the Spectro-Polarimetric High-contrast imager for Exoplanets REsearch (SPHERE; Beuzit et al. 2019) instrument on the Very Large Telescope (VLT), Maire et al. (2016) concluded that the 1.0–1.6 μm spectrum of HD 1160 B best matched that of a M6.0$^{+1.0}_{-0.5}$ dwarf. Unlike Nielsen et al. (2012), they did not find unusually red colours for either companion. They also found higher estimates for its mass; 79^{+65}_{-40} $M_{\rm Jup}$ based on its luminosity and 107^{+59}_{-38} $M_{\rm Jup}$ based on its effective temperature. The wide range of possible masses is driven by the uncertain age used,

100^{+200}_{-70} Myr, which was chosen due to the lack of reliable age indicators with the upper limit given by the 300 Myr predicted main-sequence lifetime of an A0 star (Siess, Dufour & Forestini 2000).

Garcia et al. (2017) also observed the HD 1160 system, using the Subaru Coronagraphic Extreme Adaptive Optics (SCExAO; Jovanovic et al. 2015a) instrument and the Gemini Planet Imager (GPI; Macintosh et al. 2014). They too found that HD 1160 B has typical colours for a mid-M dwarf and assign it a spectral type of M5.5$^{+1.0}_{-0.5}$, in good agreement with Maire et al. (2016), and rule out earlier spectral types. Considering a range of different evolutionary models, they report two different possible system ages; 20–125 Myr if HD 1160 A is considered alone, and 80–125 Myr if HD 1160 A, B, and C are considered jointly. These lead to mass values for HD 1160 B of 35–90 $M_{\rm Jup}$ and 70–90 $M_{\rm Jup}$, respectively. However, they note that the derived mass of HD 1160 B is highly dependent on its surface gravity and age. Garcia et al. (2017) further found that HD 1160 B likely has approximately solar metallicity, which is consistent with almost all systems in the solar neighbourhood (e.g. Dias et al. 2002).

Based on its *Gaia* kinematics, Curtis et al. (2019) found that the HD 1160 system could be part of the Pisces-Eridanus stellar stream, indicating an age on the order of $\sim$120–135 Myr if this were to be confirmed (Meingast, Alves & Fürnkranz 2019; Röser & Schilbach 2020).

The most recent spectral characterization of HD 1160 B was carried out by Mesa et al. (2020), who again observed the system with SPHERE and found it to have a peculiar spectrum that is not well matched by any spectra in current spectral libraries, but concluded a spectral type of M5-M7 based on the best fits to individual spectral bands. They propose that this peculiarity could be explained by the presence of dust in its photosphere, or if it has a young age and is not yet fully matured. By fitting the spectrum of HD 1160 B with atmospheric models and considering alkali lines that become weaker at lower surface gravities, Mesa et al. (2020) found a low surface gravity of log(g) = 3.5–4.0 dex. This suggests that HD 1160 B may actually have a young age of 10–20 Myr, and a mass of $\sim$20 $M_{\rm Jup}$, in contrast to previous results. However, they noted that they cannot rule out older ages.

While the studies above explored the spectrum of HD 1160 B, it was also the target of a variability monitoring search by Sutlieff et al. (2023). As described in Section 1, they found 8.8 per cent semi-amplitude variability with a period of $\sim$3.24 h in the differential L-band white-light curve of HD 1160 B during a pilot study combining the technique of differential spectrophotometry with the dgvAPP360 coronagraph. They attribute this variability to heterogeneous features in the atmosphere of the companion, such as clouds or cool star spots, but conclude that additional data is needed to confirm its periodicity and establish its physical explanation.

3 OBSERVATIONS

We observed the HD 1160 system on the nights of 2020 September 25 (03:27:31–11:16:14 UT) and 2020 September 26 (03:20:16–10:46:09 UT) using the 2 x 8.4-m Large Binocular Telescope (LBT) at the Mount Graham International Observatory, Arizona. On the left-hand side aperture of the LBT, we used the dgvAPP360 coronagraph (see Section 1) in combination with the Arizona Lenslets for Exoplanet Spectroscopy (ALES) IFS (Skemer et al. 2015; Hinz et al. 2018; Stone et al. 2018). ALES is located in the focal plane of the LBT mid-infrared camera (LMIRcam; Wilson et al. 2008; Skrutskie et al. 2010; Leisenring et al. 2012) and mounted inside the LBT Interferometer

(LBTI; Defrère et al. 2015; Hinz et al. 2016; Ertel et al. 2020), which uses the LBTI adaptive optics (AO) system to provide a Strehl ratio up to 90 per cent at 4 μm (Hinz et al. 2012; Bailey et al. 2014b; Pinna et al. 2016, 2021). These observations were obtained using the ALES *L*-band prism, providing $R \sim 40$ spectroscopy over a 2.8–4.2 μm wavelength range simultaneously, with a 2.2 arcsec x 2.2 arcsec field of view and plate scale of ∼35 mas spaxel^{-1} (Skemer et al. 2018).

The first night of these LBT/ALES + dgvAPP360 observations has previously been described by Sutlieff et al. (2023). On the second night, we obtained 2000 ALES frames with 5.4 s of integration time per frame, ensuring that the stellar PSF remained unsaturated in each frame. The total time on-target was therefore 10 800 s or 3 h (compared to ∼3.32 h on the first night, over 2210 frames of the same integration time; Sutlieff et al. 2023). However, this on-target integration time is spread out over ∼7.43 h due to time spent on nodding, wavelength calibrations, and readout time. When we combine both nights of data, the total on-target integration time is 22 734 s (6.32 h) over a timescale of 112 718 s (∼31.31 h, ∼1.30 d). To enable background subtraction, both nights used an on/off nodding pattern, switching position every 10 min except when interrupted by an open AO loop or to take wavelength calibrations. We also obtained six wavelength calibrations at irregular intervals throughout the night, and dark frames at the end of the night with the same exposure time as the science and calibration frames. At a separation of ∼0.78 arcsec, HD 1160 B remained in the coronagraphic dark hole of the dgvAPP360 at all wavelengths throughout the observations, while HD 1160 C was beyond the 2.2 arcsec × 2.2 arcsec field of view of ALES at ∼5.1 arcsec.

On the right-hand side LBT aperture, we used the Potsdam Echelle Polarimetric and Spectroscopic Instrument (PEPSI), a fibre-fed white-pupil echelle spectrograph (Strassmeier et al. 2015, 2018c). We obtained high resolution ($R = 50\,000$) optical spectra on both nights using the 300 μm diameter PEPSI fibre, which operates over a wavelength range of 383–907 nm. This fibre has a diameter of 2.25 arcsec which encompasses the angular separation of HD 1160 B from HD 1160 A (∼0.78 arcsec), so the obtained PEPSI spectra are combined spectra of both objects. HD 1160 C was located outside of the fibre at a separation of ∼5.1 arcsec. Data were obtained with the first three and the sixth PEPSI cross dispersers (CDs), which cover wavelength ranges of 383.7–426.5, 426.5–480.0, 480.0–544.1, and 741.9–906.7 nm, respectively, but not with the fourth and fifth CDs. We observed using two CDs at any given time; the sixth CD was always in use, and was paired with one of the other three on a rotating cycle. The total on-target integration times obtained with each CD were 14 713, 14 761, 14 666, and 44 723 s for CDs 1, 2, 3, and 6, respectively.

On the second night, no time was lost to weather and the observing conditions were stable with no cloud cover. The seeing ranged from 0.7 to 1.5 arcsec. LBTI is by design always pupil-stabilized, with no instrument derotator. This means that all data are inherently obtained in pupil-stabilized mode such that the companion position rotates in the field of view with the sky. The centre of this rotation was HD 1160 A as this was used as the AO reference star. The total field rotation over the course of the night was 108.2°. This is comparable to the 109.7° of field rotation on the first night, on which the observing conditions were similarly clear with a seeing of 0.7–1.4 arcsec (Sutlieff et al. 2023). These observations were successfully scheduled during suitable nights as part of LBTI's queue scheduling, which was critical for obtaining high-quality data on two consecutive nights.

4 DATA REDUCTION AND SPECTRAL EXTRACTION

4.1 LBT/ALES + dgvAPP360 data processing

Our goal is to use the LBT/ALES + dgvAPP360 observations to characterize HD 1160 B by measuring both its spectrum and its time variability. We therefore need to construct a flux-calibrated spectrum of the companion by summing the observations in the time dimension, and a 'white-light' curve of the companion by summing the observations in the wavelength dimension.

Several data processing steps are required to convert the raw ALES data from 2D grids of micro-spectra on the detector into 3D image cubes of x,y-position and wavelength and prepare them for our analyses (Briesemeister et al. 2019; Doelman et al. 2022; Stone et al. 2022). The data from the first night of LBT/ALES + dgvAPP360 observations was previously processed (for a time variability study only) by Sutlieff et al. (2023). We reprocessed this first night of data here following the same method as Sutlieff et al. (2023), and also used this approach for the data from the second night to ensure consistency between the two epochs. We briefly summarize the steps in this process here. We first used the sky frames from the off-source nod position to subtract the background in each frame, before extracting the micro-spectra into 3D cubes through weighted optimal extraction, where the extraction weights were defined by the wavelength-averaged spatial profiles of the micro-spectra in the sky frames (Horne 1986; Briesemeister et al. 2018; Stone et al. 2020). Next, the data were wavelength calibrated using four narrow-band filters operating upstream of the ALES optics. Each of these filters produced a single-wavelength spot on the LMIRcam detector. We performed the wavelength calibration for the 63×67 micro-spectra in the ALES grid by fitting the positions of these four spots with a second-order polynomial to derive the necessary wavelength solution (Stone et al. 2018, 2022). This process produced 3D wavelength-calibrated data cubes of *x*- and *y*-position (63×67 pixels), and wavelength λ, with 100 wavelength channels spanning the 2.8–4.2 μm wavelength range of ALES.

Continuing to follow the data reduction method of Sutlieff et al. (2023), we removed eight frames from the first night that were unsuitable as the AO loop opened during the exposure. No frames were removed from the data set from the second night. We then performed a bad pixel correction for each frame before applying a flat-field correction. The flat frame used for this was created from images obtained in the off-source nod position. ALES images also contain systematic time-varying row and column discontinuities caused by the intersection of the ALES micro-spectra with the channels of the LMIRcam detector (Doelman et al. 2022). To correct for the column discontinuities, we first masked HD 1160 A and B in each frame before fitting third-order polynomials to each column. These values were then subtracted and the process was repeated for each row to remove the row discontinuities. The frames were then shifted using a spline interpolation to centre the star in each frame and derotated using their parallactic angles to align them to north. A final image from the second night, obtained by median-combining every frame in the 3.59–3.99 μm range in both time and wavelength, is shown in the top panel of Fig. 1. Both HD 1160 A and B are clearly visible.

As the data were obtained in pupil-stabilized mode, we could have applied post-processing algorithms reliant on angular diversity (e.g. Angular Differential Imaging; Marois et al. 2006) to further remove quasistatic speckle noise and increase the S/N of the targets. However, we chose not to do this so that we could make use of the stellar PSF provided by the dgvAPP360 as a simultaneous photometric reference
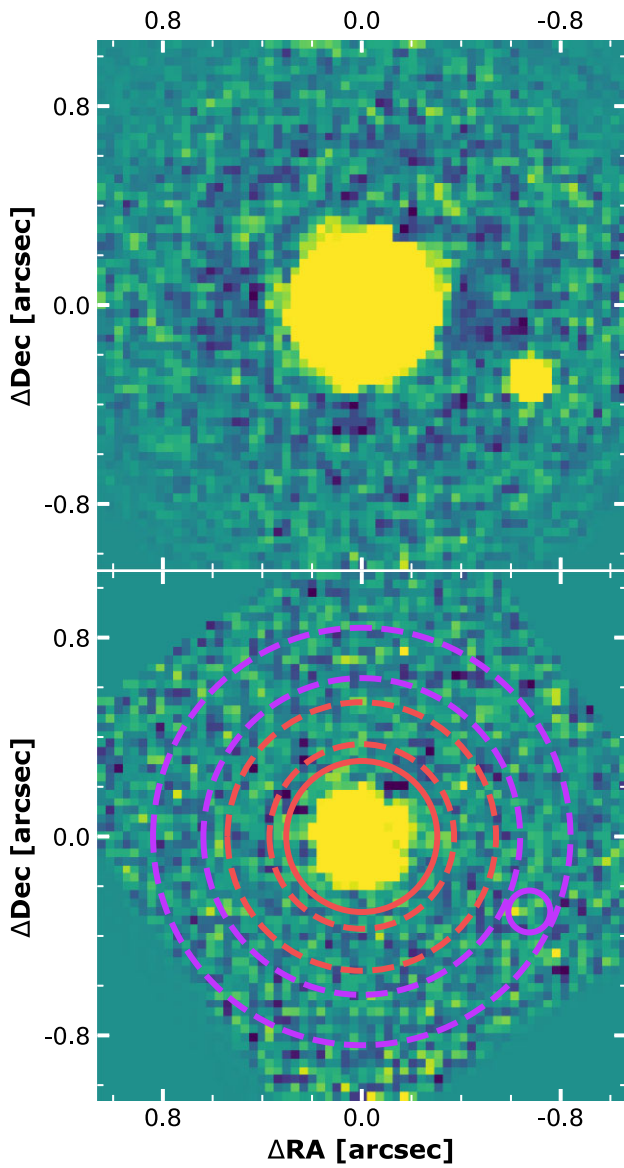
Figure 1. Top panel: the final LBT/ALES + dgvAPP360 image of the HD 1160 system from the second night, produced by taking the median combination of all frames in the 3.59–3.99 μm range over both time and wavelength. This image covers a total integration time of 10 800 s (3 h). Bottom panel: A single frame of data from the 3.69 μm wavelength channel, overplotted with the apertures and annuli used to obtain flux and background measurements for the host star HD 1160 A (in orange) and companion HD 1160 B (in purple). The dashed lines indicate the background annuli. Each image uses a different arbitrary logarithmic colour scale, and both are north-aligned, where north is up and east is to the left.

when characterizing the variability of HD 1160 B in Section 5. If we had applied an ADI-based algorithm the stellar PSF would have been removed, meaning there would be no photometric reference with which to divide out time-varying systematics from the companion flux.

4.1.1 Photometric extraction

Once the data had been fully processed to correct for the systematic discontinuities, we extracted simultaneous aperture photometry of

HD 1160 A and B, again following the approach of Sutlieff et al. (2023). Although some of the 100 ALES wavelength channels are not suitable for analysis (see Sections 5.1 and 6.1), we nonetheless performed this step for every frame in each of the 100 channels to allow a selection to be carried out at a later stage in the process. To do this, we extracted photometry in circular apertures with radii of 9 pixels (3.1 λ/D) for HD 1160 A and 2.5 pixels (0.9 λ/D) for HD 1160 B. The background flux was near zero following the removal of the row and column discontinuities in the previous section. However, we nonetheless estimated the residual background at the locations of the star and companion such that we could correct our flux measurements for any remaining offset. The background flux at the location of HD 1160 A was estimated by extracting photometry in a circular annulus with inner and outer radii of 11 and 16 pixels, respectively. The drift of the star combined with the rotation of the field over the course of the night means that HD 1160 B was close to the edge of the field of view in some frames, meaning that we could not use a similar annulus to estimate the background at its location. Instead, we did this by masking HD 1160 B and then extracting photometry in another annulus centred on the star, this time with a 6-pixel width around the radial separation of HD 1160 B (Biller et al. 2021; Sutlieff et al. 2023). We show these apertures and annuli overplotted on a single frame of data in the bottom panel of Fig. 1. We then corrected our aperture photometry of the star and companion by subtracting the mean counts per pixel in the corresponding annulus multiplied by the area of the respective aperture.

This extracted spectrophotometry of HD 1160 A and B is used to investigate the time variability of HD 1160 B in Section 5 and its spectrum in Section 6.

4.2 PEPSI data processing

In this paper, we aim to use the LBT/PEPSI observations to characterize the physical properties of host star HD 1160 A. The PEPSI data were reduced using the Spectroscopic Data Systems for PEPSI (SDS4PEPSI) generic package written in C++ under Linux and based on the 4A package for processing data from the SOFIN spectrograph on the Nordic Optical Telescope (Ilyin 2000; Strassmeier, Ilyin & Steffen 2018a; Strassmeier, Ilyin & Weber 2018b; Keles et al. 2022). SDS4PEPSI applied a fully automated set of standardized data reduction steps to the raw data, including CCD bias removal, photon noise estimation, flat-field correction, and scattered light subtraction. It then performed a weighted optimal extraction of the spectral orders to maximize the S/N of the target, and then performed wavelength calibration. The spectra were then normalized to the continuum by fitting the extracted spectral orders with a 2D smoothing spline on a regular grid of CCD pixels and echelle order numbers, and then shifted to the stellar rest frame. Each of these steps carried out by SDS4PEPSI is described in full detail by Strassmeier et al. (2018a). Finally, we combined the spectra from all of the exposures obtained with a given CD by interpolating them to the same wavelengths and summing them according to their weights, where the weights are defined as the inverse of the noise.

5 ANALYSING THE VARIABILITY OF HD 1160 B

In this section, we use the aperture photometry of HD 1160 A and B obtained in Section 4.1.1 to explore the time variability of HD 1160 B via the technique of differential spectrophotometry. This method applied using the dgvAPP360 coronagraph was first described by Sutlieff et al. (2023). While we are interested in the intrinsic

variability arising from the atmosphere of the companion, the raw flux that we obtained through aperture photometry is inherently polluted by additional variability caused by Earth's atmosphere and systematics originating from the instrumentation. This unwanted variability can be mitigated using an independent, simultaneous photometric reference, but this is generally problematic for ground-based variability studies of high-contrast companions, as field stars are rarely available and focal-plane coronagraphs block the host star in order to allow companions to be detected (e.g. Mawet et al. 2012; Ruane et al. 2018). The dgvAPP360 coronagraph uniquely enables host stars and their companions to be imaged simultaneously, thus we can use the simultaneous aperture photometry of HD 1160 A as a photometric reference to remove variability arising from non-astrophysical sources external to HD 1160 B (Doelman et al. 2020, 2021; Sutlieff et al. 2023). As HD 1160 A does not fit into any known category of variable star and Sutlieff et al. (2023) previously found no evidence for variability in HD 1160 A above the 0.03 per cent level in *TESS* observations over a 51 d baseline, we proceed with the assumption that HD 1160 A does not have intrinsic variations of its own at longer wavelengths.

5.1 ALES wavelength channel selection

The first step in the process of making a differential white-light curve for HD 1160 was to select which wavelength channels should be included. A benefit of the spectrophotometric approach is that channels with low target S/N or issues that could introduce false variability signals can be excluded, allowing the light curve precision to be maximized. Our data cubes consist of 100 wavelength channels ranging from 2.8 to 4.2 μm. However, wavelength channels at the start and end of this range are unsuitable for analysis as the photometry is contaminated by flux from the neighbouring spaxel in the dispersion direction, and those in the ~3.25–3.5 μm wavelength range are significantly impacted by absorption caused by the glue molecules in the dgvAPP360 (Otten et al. 2017; Doelman et al. 2021, 2022). Sutlieff et al. (2023) selected the 30 wavelength channels in the 3.59–3.99 μm range that had a high target S/N for inclusion in their time variability analysis of the first night of data. We therefore chose to use these same channels for our variability analysis in this paper such that we could directly compare the light curves from each night of data. We discuss the spectral data obtained on each night over the full 2.8–4.2 μm wavelength range covered by ALES in Section 6.1.

5.2 Differential spectrophotometric light curves

We produced our differential white-light curve of HD 1160 B following the technique presented by Sutlieff et al. (2023). First, we separately prepared white-light time series for HD 1160 A and HD 1160 B. We did this by taking the median combination of the photometry for each object over the 30 wavelength channels chosen in the previous section, thereby obtaining a single white-light measurement for each object at each time. These are shown in grey in the top two rows of Fig. 2, and binned to 18 min of integration time per bin in blue and yellow for the host star and companion, respectively. The time series shown here are plotted on the same axes and were normalized over the full sequence, including both epochs, to allow comparison between each night. Aside from the change in the normalization, the data points on the first night are identical to those of Sutlieff et al. (2023). Thus, at this point, our analysis of the first night of observations deviates slightly from that presented by Sutlieff et al. (2023).

The gaps in integration time in the unbinned data are due to the on/off nodding pattern used when observing, and the unequal *x*-uncertainties on the binned data points occur where the bins overlap multiple nods. To produce a differential white-light curve, we then divided the unbinned, unnormalized flux of HD 1160 B by that of HD 1160 A. This raw differential light curve is plotted unbinned in grey, and binned in purple, in the third row of Fig. 2. We also plot a closer view of the same binned light curve in the fourth row. We calculated the errors on the binned fluxes by taking the 1.48 × median absolute deviation (MAD) of the fluxes in each time bin, then dividing these values by $\sqrt{N-1}$, where N is the number of frames per bin. Dividing the two time series in this way has the effect of removing most of the variability due to shared systematics arising from the instrumentation or telluric effects. HD 1160 A is known to be non-varying to at least the 0.03 per cent level (Sutlieff et al. 2023), so remaining variability trends in this differential light curve are therefore only those arising from HD 1160 B itself and from any contaminating systematics that are not shared by the star and the companion.

5.3 Detrending

In this section, we attempt to fit and remove several residual (i.e. non-shared) systematic trends from the differential light curve, with the aim of producing a detrended differential light curve containing only the intrinsic variability of HD 1160 B. These residual systematics are likely due to differences in brightness, colour, or position of the companion and host star, and can arise from both instrumental and telluric sources (e.g. Broeg, Fernández & Neuhäuser 2005; Pont, Zucker & Queloz 2006; Gibson et al. 2012; de Mooij et al. 2013; Diamond-Lowe et al. 2018; Panwar et al. 2022a,b). Here, we applied a multiple linear regression including six different possible sources of systematics as decorrelation parameters. These parameters are shown plotted against time in hours after midnight, for each epoch, in Fig. 3. Sutlieff et al. (2023) found that airmass and external air temperature were the parameters that were the most correlated with the differential light curve from the first night alone, so we chose to include both of these again here. We also again included the x- and y-pixel positions of HD 1160 A and B in the original images, before centering and rotational alignment were carried out. These parameters probe any remaining systematics arising from the response of the detector or other instrumental effects. The sharp jumps in position seen in Fig. 3 arise from manual positional offsets performed during the observing sequence to ensure the star did not drift too far from the centre of the small field of view. We further considered including wind speed and wind direction, but Sutlieff et al. (2023) found that wind speed and wind direction were not significantly correlated with the trends in the light curve from the first night. We found that this was also the case for the second night, so chose not to include these as parameters in the linear regression here. Thus, in addition to the different normalization applied in Section 5.2, this is the other point at which our analysis of the first night of observations is slightly different to that of Sutlieff et al. (2023).

We used a multiple linear regression (as implemented in the SCIKIT-LEARN Python package; Pedregosa et al. 2011) to simultaneously fit these six decorrelation parameters to the differential white-light curve of HD 1160 B. This process was carried out for the light curve on each night separately, in case the systematics induce different trends on each night. The resulting model fits are shown in dark green in the top panels of Fig. 4, overplotted on the raw differential white-light curves (in grey). The corresponding coefficients and intercept
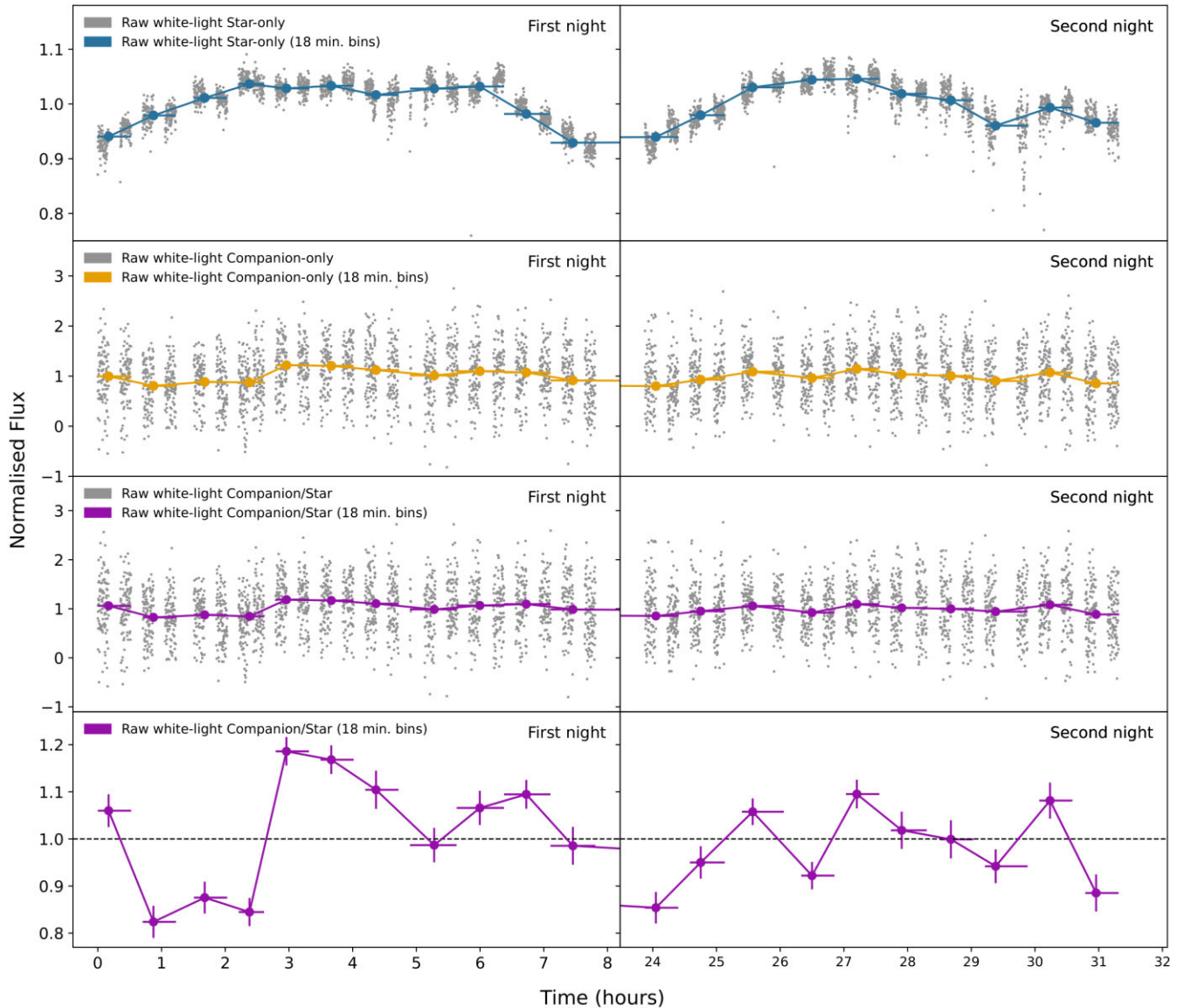
Figure 2. Top two rows: the raw white-light fluxes of host star HD 1160 A and companion HD 1160 B from both nights are plotted in grey, and binned to 18 min of integration time per bin in blue and yellow, respectively. The time series were normalized over the full time series covering both epochs, and consist of the data in the 3.59–3.99 μm wavelength range. The data from the first night is reproduced from Sutlieff et al. (2023), but the normalization is different here. Bottom two rows: the raw differential white-light curve obtained by dividing the unnormalized, unbinned companion flux by that of the star, shown unbinned in grey and binned in purple. The bottom row shows a zoomed-in view of the binned version. This division removes variability shared by both the star and the companion from the companion flux, leaving a differential light curve containing only variability arising from the companion's atmosphere and non-shared systematics.

of these two models are given in Table 2. We detrended the two differential white-light curves by dividing by these linear regression models, respectively. The final detrended differential white-light curves are plotted in the bottom panels of Fig. 4, alongside the raw differential white-light curves for comparison (in light purple, reproduced from the bottom panel of Fig. 2). Sutlieff et al. (2023) also presented detrended differential light curves for the first night in each of the 30 individual wavelength channels that were combined to obtain white-light flux measurements for HD 1160 A and B. To allow a comparison to their results, we also produced the detrended differential light curves in each wavelength channel for each night. These light curves are shown in Fig. 5, binned to 18 min of integration time per bin. The small differences in the wavelengths of each channel between nights arise from the different wavelength solution

required for the wavelength calibration of each night of data (see Section 4.1).

5.4 Period analysis and light curve precision

Sutlieff et al. (2023) identified sinusoidal-like variability in the first night of the detrended differential white-light curve of HD 1160 B and produced a Lomb-Scargle periodogram to search for periodicity. They then fit a sinusoid to the light curve and measured the period of this variability as 3.239 h. This trend is still present in the first night of our new light curve (Fig. 4). However, while some individual data points appear to deviate from a flat line, it is not visually clear whether or not the detrended differential white-light curve from the second
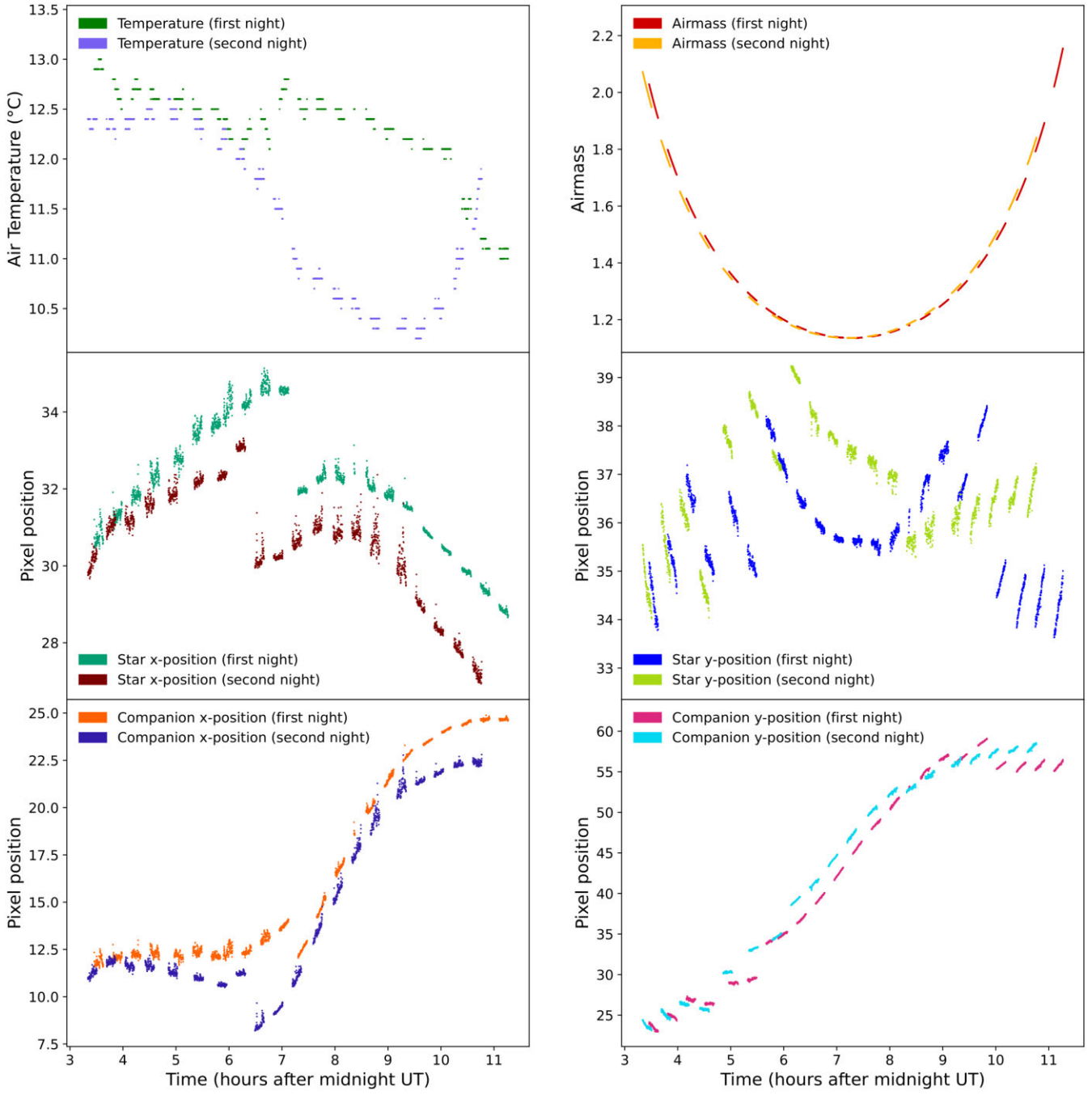
Figure 3. The six decorrelation parameters used in the linear regression to detrend the differential white-light curve of HD 1160 B, shown for both nights. To allow the trends at each epoch to be overplotted and compared, 24 h has been removed from the *x*-axis for the second night. As with the time series photometry, the gaps in the data arise from the use of the on/off nodding pattern. The top two panels show the air temperature in °C and the airmass as a function of time. The remaining four panels show the x- and y-positions (in pixels) of host star HD 1160 A and companion HD 1160 B in the original 3D image cubes (i.e. before spatial and rotational alignment) as a function of time. The large jumps in these positions were caused by manual offsets applied to maintain the central location of HD 1160 A within the small field of view, and the slowly varying trends arise from lenslet array flexure as the telescope rotates. For HD 1160 B, the rotation of the field of view itself (109.7° and 108.2° for the first and second nights, respectively) induces an additional component to its positional trends.

night is also variable. The maximum normalized flux is 1.07, but the RMS of the light curve is 0.035. We therefore carried out a similar analysis to Sutlieff et al. (2023) to search for periodic variability using periodograms.

We produced periodograms for the unbinned detrended differential white-light curve using the Lomb-Scargle algorithm (Lomb 1976; Scargle 1982). These are shown in the left-hand panels of Fig. 6;

the top panel was produced using both nights combined, while the centre and bottom panels show the periodograms produced using only the data from the first and second nights, respectively. Each of these power spectra has been normalized by dividing them by the variance of the data points in the light curve (Horne & Baliunas 1986). The blue dashed line is the power threshold that corresponds to a false-alarm probability of 0.1 (i.e. 10 per cent), and the horizontal
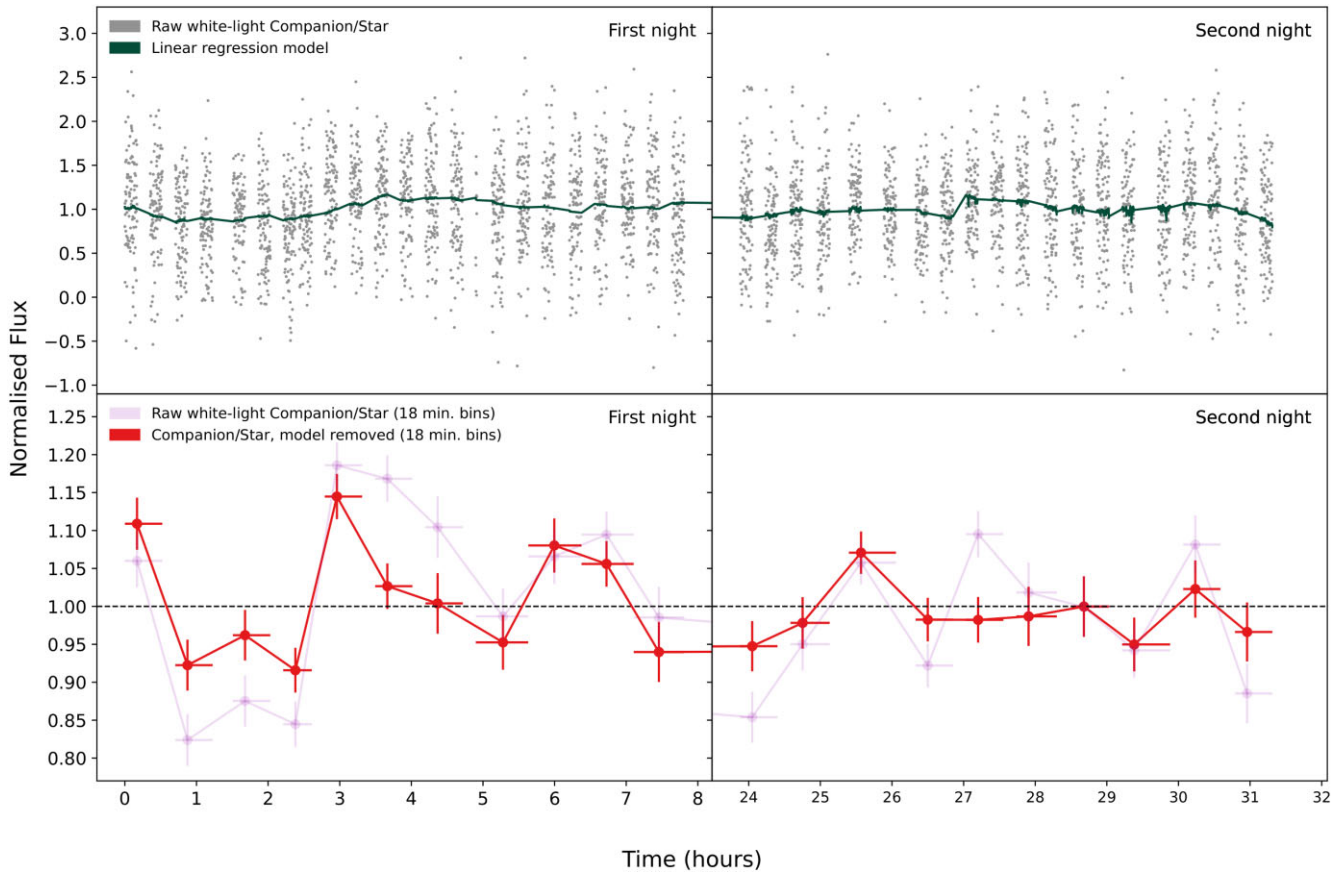
Figure 4. Top panel: the model, in dark green, produced when a multiple linear regression is applied to the raw white-light differential light curves from each night using the decorrelation parameters from Fig. 3. The corresponding coefficients and intercept of each model are given in Table 2. The raw differential white-light curve is shown in grey, reproduced from the third panel of Fig. 2. Bottom panel: the detrended differential white-light curve, in red and binned to 18 min of integration time per bin, obtained by dividing the raw differential light curve by the linear regression models above. The binned version of the raw differential white-light curve from the bottom panel of Fig. 2 is also shown for comparison in purple.

Table 2. The decorrelation parameters x_i included in the linear regression used to detrend the differential white-light curve of HD 1160 B at each epoch. The resulting linear model fit was given by $y = (\sum_{i=1}^{n} c_i x_i) + c_0$, where c_0 is the intercept and c_i are the coefficients of each parameter. The parameters are ordered by the magnitude of the corresponding coefficients on the first night.

Parameter (x_i)	Value, 1st night (c_i)	Value, 2nd night (c_i)
Airmass	0.34590456	− 0.46758893
Air temperature	0.11689032	− 0.12725877
Star x-position	0.04596314	− 0.08979261
Star y-position	− 0.04426898	0.02947633
Companion x-position	− 0.02499303	0.00674422
Companion y-position	0.01966123	− 0.01849457
Intercept (c_0)	− 1.23206397	5.45860550

brown dotted line on the periodogram for the first night is the power threshold for a false-alarm probability of 0.01 (i.e. 1 per cent).

We find that the strongest peak in the periodogram of the first night is at approximately the same period as Sutlieff et al. (2023), with a period of 3.227 h, peak power of 14.67, and false-alarm probability of 0.009. This slight difference in period is due to the different normalization used here and the different linear regression model produced by not including wind speed and wind direction as decorrelation parameters. The second strongest peak in this

periodogram, with a period of 1.370 h, peak power of 13.26, and false-alarm probability of 0.035, does not appear to be harmonic with the strongest peak. However, there are no significant peaks present in the periodograms of the second night or of both nights combined. All of the features in these periodograms have false-alarm probabilities greater than 0.5. When the light curves are combined, the periodicity in the first night appears to be diluted by an absence of constructive addition from periodicity in the second night, causing there to be no significant peaks in the combined periodogram.

As the data are irregularly sampled, with large gaps due to the nodding pattern and the break between the two nights, we also produced periodograms for the window functions for each night and both nights together to check for potential artefacts arising from this irregular sampling (e.g. Fuhrmeister et al. 2019; Apai, Nardiello & Bedin 2021). The window functions were calculated by producing an evenly sampled array consisting of ones at times where data exists and zeros where it does not. The periodograms of these window functions are shown in the right-hand panels of Fig. 6. We find that there are no significant peaks at periods >1 h in the window function periodograms for the first and second nights individually. This suggests that the strong peak that we detect at 3.227 h in the periodogram of the first night light curve is not an artefact caused by the irregular sampling of the data. In both cases, there are significant peaks present at shorter periods (<1 h), which is likely a reflection of the nodding pattern used when obtaining the data. These are also
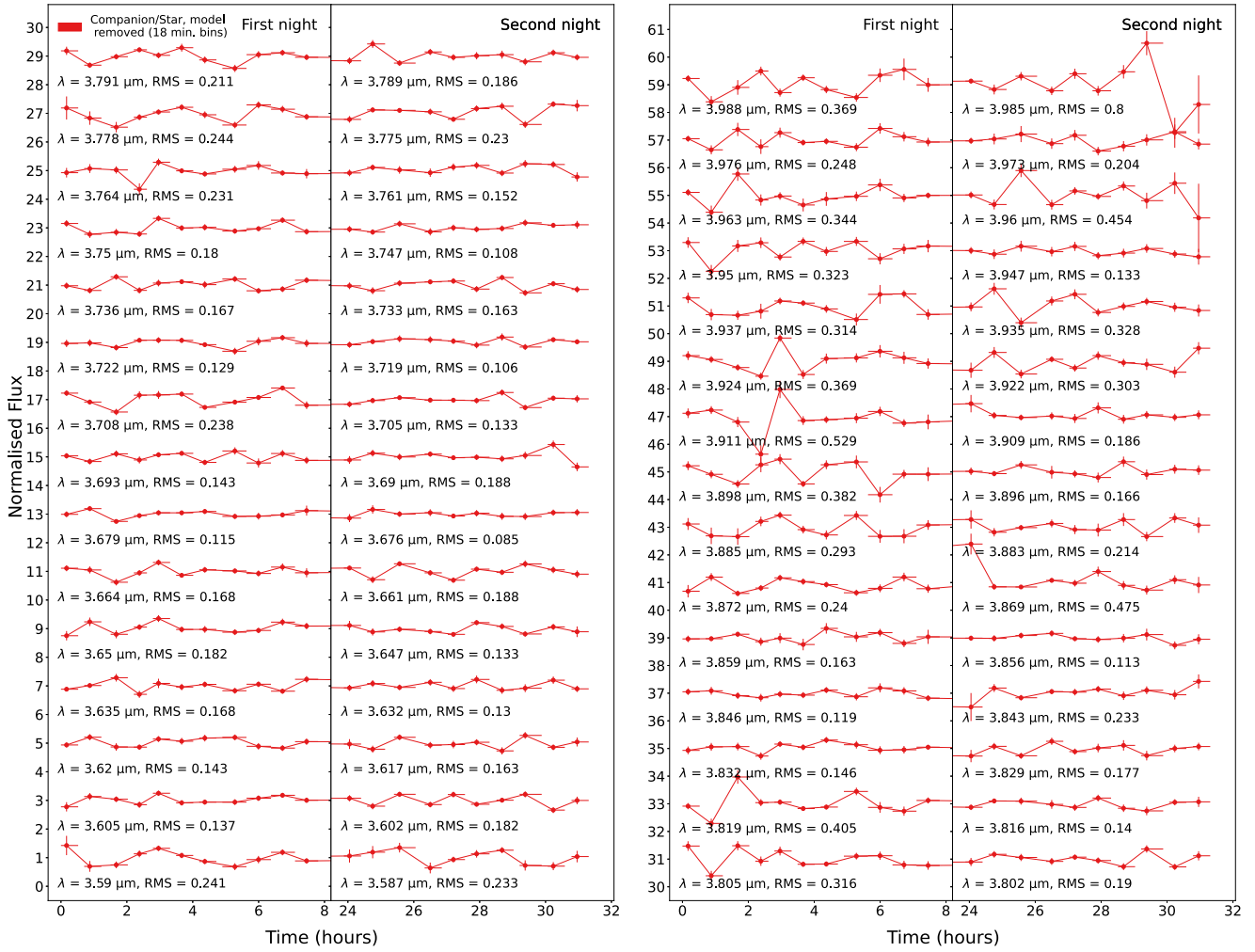
Figure 5. The detrended differential light curves in each of the 30 individual wavelength channels that were combined to obtain white-light flux measurements for HD 1160 A and B. All light curves are binned to 18 min of integration time per bin, and each light curve is offset by 2 on the *y*-axis from the previous wavelength to spatially separate them in the figure.

present for the both nights combined case along with several peaks at longer periods, which we interpret as harmonics of the nodding that appear due to the large gap between the two nights, but none align with the 3.227 h peak from the first night.

We also carried out a comparative analysis of the precision achieved in each detrended differential white-light curve. When estimating the precision achieved for the first night, Sutlieff et al. (2023) first fitted and removed the observed periodic variability signal from the light curve. They did this using a non-linear least-squares approach, assuming that it followed a sinusoidal trend and using the period of the highest peak in the periodogram as an initial guess for the fit. They then measured the precision using the residual light curve. As we do not detect a clear periodicity in the light curve from the second night, we could not do this here if we wished to compare the precision achieved on each night. We therefore instead performed our assessment of the precision using the detrended differential white-light curves from each night, and both nights combined, noting that any variations intrinsic to HD 1160 B would make these values appear higher and therefore above the true limiting precision. We did this by following the approach used by Kipping & Bakos (2011) and Sutlieff et al. (2023) for assessing the impact of correlated noise on time-series data. First, we binned our detrended differential white-

light curves into a range of different bin sizes. We then renormalized the resulting binned light curves and subtracted one to centre them around zero, before measuring the root mean square (RMS) of each one. We plot these values as a function of bin size for each light curve in Fig. 7. The black line shows the expectation of independent random numbers with increasing bin size, $\sigma_N = \sigma_1 N^{-0.5} [M/(M-1)]^{0.5}$, where N is the bin size and M is the number of bins (Kipping & Bakos 2011). If we take the RMS values at each night for the bin size that we used for our binned white-light curves in Figs 2 and 4 (i.e. 200 frames per bin, or 18 min of integration time), we find RMS values of 0.075 and 0.035 for the first and second nights, respectively. The RMS value at this bin size for the light curve covering both nights combined is 0.060. The higher RMS for the first night (and both nights combined) reflects the higher variability that we see here compared to the second night. We discuss these results further in Section 8.1.

6 SPECTRAL ANALYSIS OF HD 1160 B

In addition to investigating the brightness fluctuations of HD 1160 B, we also extracted its spectrum on each night to allow us to
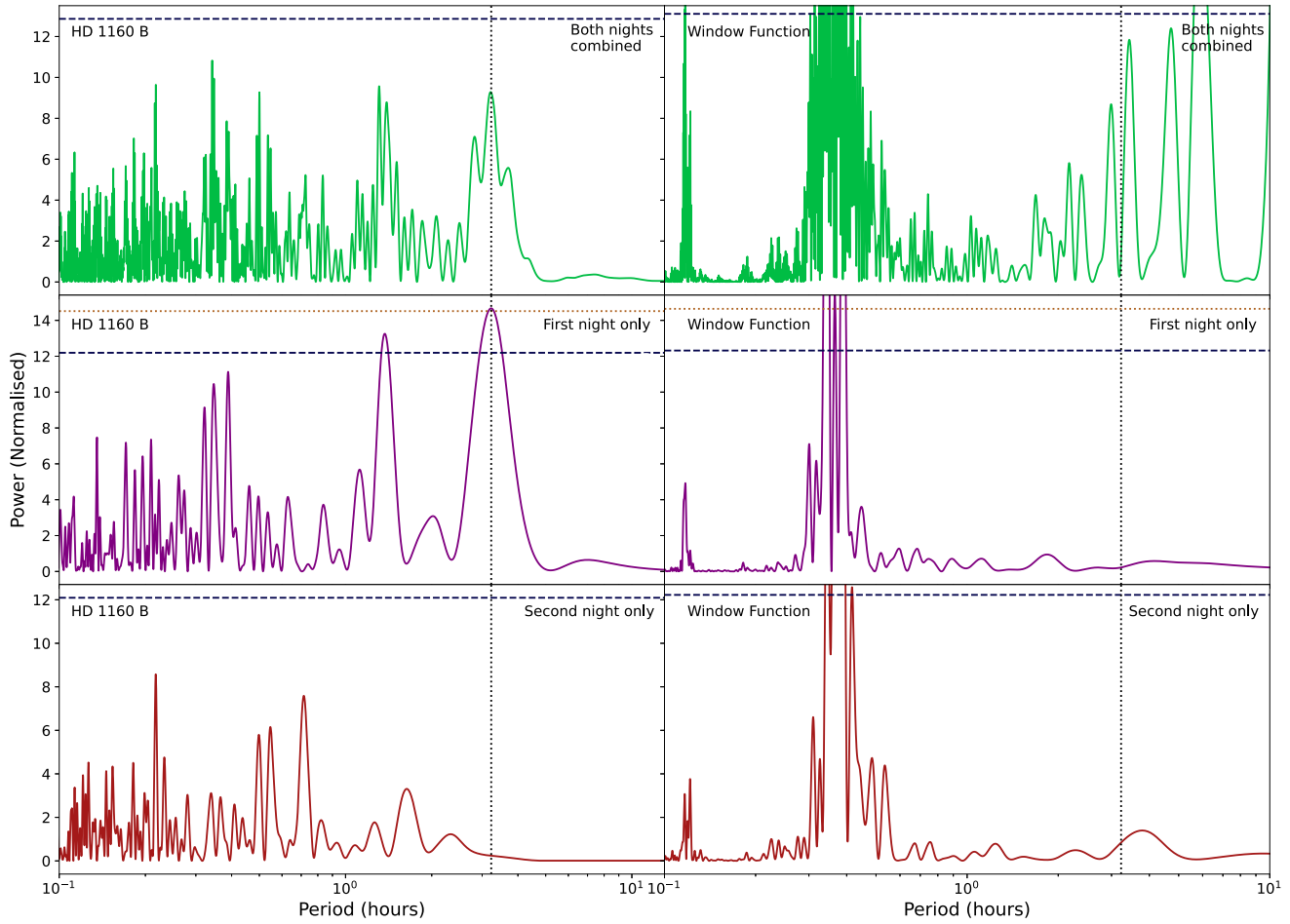
Figure 6. The left-hand panels show the Lomb-Scargle periodograms produced using the unbinned, detrended differential white-light curves from Fig. 4. The top panel shows the periodogram for the full light curve over both nights, whereas the centre and bottom panels are those for the light curves of the first and second nights only, respectively. The right-hand panels show the periodograms of the corresponding window functions. The blue dashed lines indicate the power threshold corresponding to a false-alarm probability of 0.1 (10 per cent), and the horizontal brown dotted line is that for a false-alarm probability of 0.01 (1 per cent). The vertical dotted line highlights the 3.227 h period of the strongest peak in the periodogram for the first night.
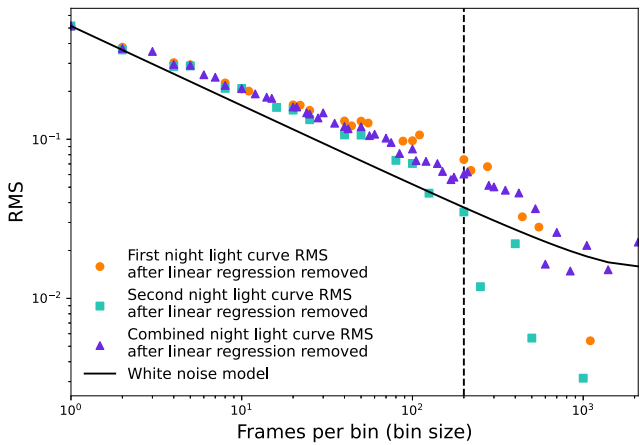
Figure 7. The RMS of the binned detrended differential white-light curve of HD 1160 B for the first and second nights, respectively, without the removal of any periodic variability. The theoretical white noise model as a function of bin size is also shown. This was calculated using the bin sizes used for the both nights combined light curve. The vertical dashed line indicates a bin size of 200, as used for our binned white-light curves in Figs 2 and 4.

characterize its physical properties through the fitting of atmospheric models.

6.1 Spectral extraction

We measured the contrast between host star HD 1160 A and companion HD 1160 B in each wavelength channel using the aperture photometry of each object obtained in Section 4.1.1. To do this, we took the median combination of these flux measurements over the time sequence, producing single flux measurements for the companion and the star at each wavelength. As with the time-dependent fluxes obtained in Section 5.2, the errors on each measurement were calculated as the $1.48 \times$ MAD of the fluxes in each wavelength channel (bin), divided by the square root of the number of frames per channel minus one. Next, we divided the companion flux at each wavelength by that of the star to produce a contrast spectrum. We carried out this process separately for each night of data.

We then converted our contrast spectra of HD 1160 B on each night into physical flux units by multiplying them by a flux calibrated spectrum of HD 1160 A. To do this, we used the Virtual Observatory SED Analyzer (VOSA; Bayo et al. 2008) to plot the Spectral Energy Distribution (SED) of HD 1160 A, including literature data from the
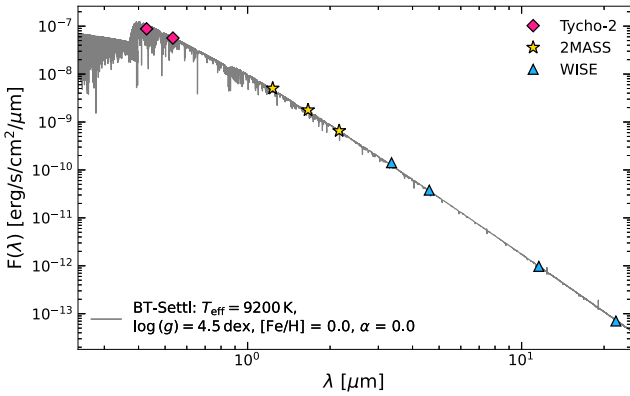
Figure 8. Literature photometry of the host star HD 1160 A from the Tycho, 2MASS, and *WISE* catalogues. The grey line shows the model fit to this photometry. The model has been convolved to a resolution of $R = 100\,000$ for visual purposes. The uncertainties are shown but are much smaller than the symbols.

2MASS (Skrutskie et al. 2006), Tycho-2 (Høg et al. 2000a,b), and *WISE* (Wright et al. 2010) catalogues. We assumed a distance of 120.7 pc and an extinction of $A_V = 0.16$ mag (Gaia Collaboration 2016, 2023). The SED was dereddened using the extinction law of Fitzpatrick (1999) and Indebetouw et al. (2005). Using a χ^2 test to fit the SED with a grid of BT-Settl models (Allard, Homeier & Freytag 2011, 2012), we selected a model with effective temperature $T_{\rm eff} = 9200$ K, surface gravity log(g) = 4.5 dex, metallicity [Fe/H] = 0.0, and alpha element abundance α = 0.0, consistent with that found by Mesa et al. (2020) using the same approach. The literature photometry of HD 1160 A and this model are shown in Fig. 8. We then convolved this model to the resolution of ALES ($R \sim$ 40; Skemer et al. 2018) and evaluated it at the wavelengths of our observations, before multiplying it by our contrast measurements to produce a flux calibrated spectrum of HD 1160 B on each night. These spectra are shown in Fig. 9, with the flux measurements from the first and second nights in blue and orange, respectively. The shaded areas indicate regions in the observed 2.8–4.2 μm wavelength range where the data are unreliable and excluded from our analysis, due to contamination from the neighbouring spaxels or the dgvAPP360 glue absorption.

We note that while the spectra from each night are in good agreement in the wavelength region redwards of the dgvAPP360 glue absorption, there appears to be a slight offset between the two nights at 3–3.2 μm, which we discuss further in Section 8.2.

6.2 Spectral fitting

Once we had obtained a flux calibrated spectrum of HD 1160 B for each night, we fit this data with atmospheric models to characterize its physical properties. We used a set of BT-Settl grid models (Allard et al. 2011, 2012, 2013) which were downloaded from the Spanish Virtual Observatory (SVO) Theory Server.[1] We restricted the models to those with effective temperatures between 400 K and 4600 K, surface gravities between 3.5 and 5.0 dex, metallicities between −0.5 and 0.5, and an α-enhancement of 0. The grid step sizes for temperature and surface gravity were 100 K and 0.5 dex, respectively, and metallicity could have values −0.5, 0, 0.3, or 0.5. We chose to restrict the range of possible surface gravities to these

---

[1] http://svo2.cab.inta-csic.es/theory/newov2/

values based on the predicted physical limitations of objects with ages and masses within the ranges found for HD 1160 B in the recent literature, which are 10–125 Myr and $\sim$20 $M_{\rm Jup}$ to 123 $M_{\rm Jup}$, respectively (Garcia et al. 2017; Curtis et al. 2019; Mesa et al. 2020). According to the isochrones and evolutionary tracks of the BT-Settl models, the surface gravities of objects with ages and masses within these constraints should always be $\geq$3.5 and $\leq$5.0 (Baraffe et al. 2015; Stone et al. 2016). Maire et al. (2016) did previously use a higher age upper limit of 300 Myr for the HD 1160 system, which would allow a HD 1160 B surface gravity of up to log(g) = $\sim$5.2, but Garcia et al. (2017) later found that such high ages were not consistent with the properties of the host star.

Each model was convolved to the $R \sim$ 40 spectral resolution of ALES and sampled at the wavelengths of our spectral data points. By fitting each model to the data, we then determined the scaling factor that minimizes the Euclidean norm of the residual vector between the two i.e. the value multiplied by each model to best match it to the companion spectrum, and calculated the χ^2 value for each fit accounting for the errors on each data point (e.g. Bohn et al. 2020a; Sutlieff et al. 2021). When calculating the χ^2 values of model fits to high-contrast IFS data, it is important to consider the effects of spectral covariance arising from oversampling during the spectral extraction process and the wavelength-dependent behaviour of speckle noise (Greco & Brandt 2016). We accounted for spectral covariances in the ALES IFS data by following the method described by Greco & Brandt (2016) to produce spectral covariance matrices for each night of data and apply them in our χ^2 calculation. The model that produced the smallest χ^2 value was then taken as the best-fitting model to the data. When performing this fitting procedure, we excluded the data points in the shaded regions of Fig. 9, which were not suitable for analysis as described in Section 6.1. We performed the fitting process three times; once each for the spectra from the first and second nights separately, and a third time considering both nights of data together. The best-fitting model in each case is shown overplotted on the companion spectrum in Fig. 10. The best-fitting model to the first night of data alone has $T_{\rm eff} = 2700$ K, log(g) = 4.5 dex, and metallicity [Fe/H] = −0.5 (purple line, Fig. 10). When the second night of data is considered alone, the best-fitting model instead has solar metallicity and is slightly cooler, with $T_{\rm eff} = 2300$ K, log(g) = 5.0 dex (red line). This is likely due to the lower flux recorded in the 3–3.2 μm region of the spectrum on this night. The effective temperature of the best-fitting model to both nights of data then lies between the two, as would be expected, with $T_{\rm eff} = 2600$ K, log(g) = 5.0 dex, and solar metallicity (green line). Using the χ^2 values of each model fit as weights, we also calculated the weighted means and sided variance estimates (i.e. statistical errors) of these atmospheric parameters using the approach of Burgasser et al. (2010a,b) and Stone et al. (2016). These results are presented in Table 3. The weighted means and their uncertainties are biased in some cases, where the preferred model fits lie at the edge of the allowed parameter range. We therefore instead report upper/lower limits in these instances.

We further inferred estimates of the radius and luminosity of the companion using the scaling factor for each model, which is equal to the squared ratio of the companion's radius and distance. As the distance to the HD 1160 system is well-known (120.7 ± 0.5 pc; Gaia Collaboration 2016, 2023), we are able to solve for radius. The luminosity can then be inferred by integrating each model over its full wavelength range and multiplying by 4π times the radius squared. These values are also shown in Table 3, where the reported uncertainties are again the statistical errors. These results are discussed further in Section 8.2.
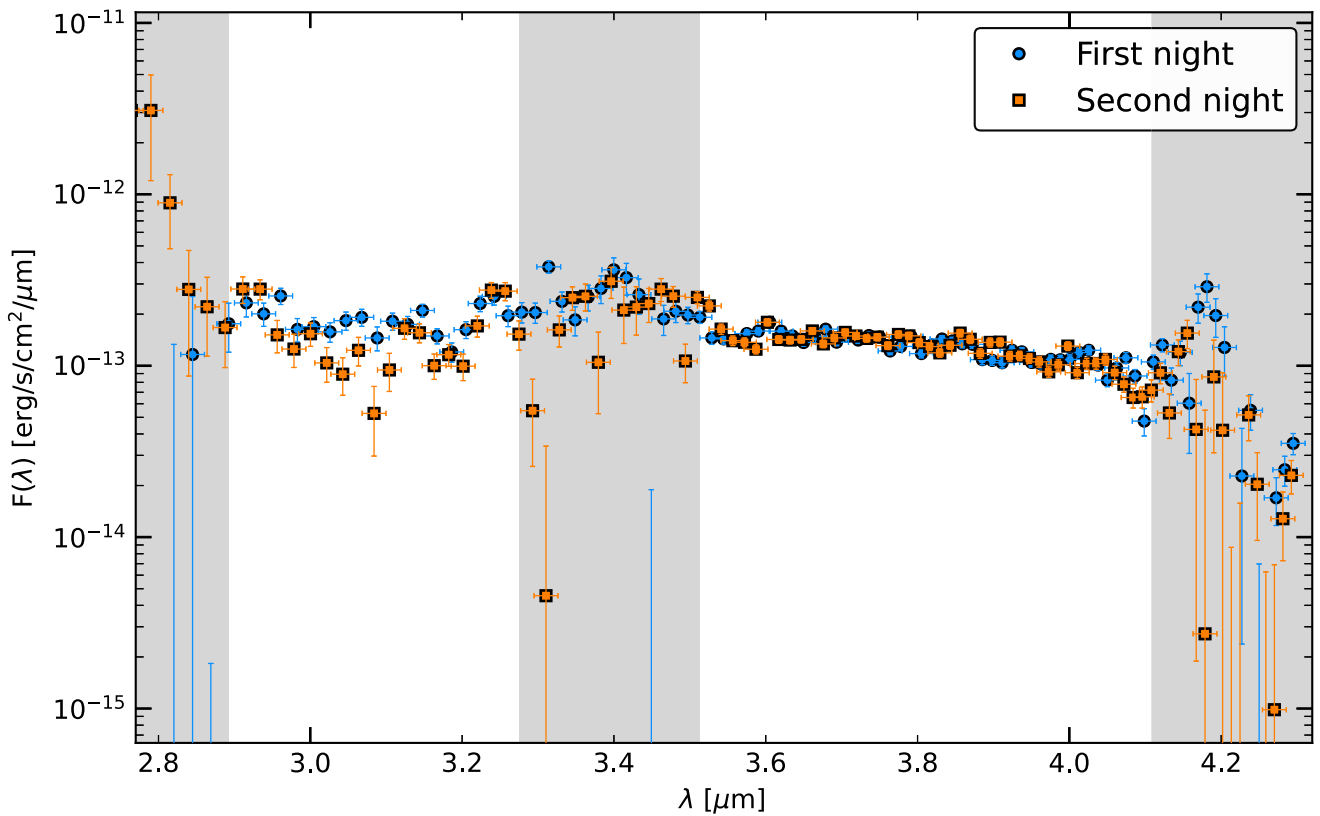
Figure 9. The flux calibrated spectrum of HD 1160 B obtained with LBT/ALES. Data points from the first and second nights are shown in blue and orange, respectively. The shaded regions indicate data points which are not suitable for analysis due to contamination arising from overlapping spectral traces or absorption caused by the carbon-carbon bonds in the glue layer of the dgvAPP360. The wavelength channels used for the variability analysis are those in the 3.59–3.99 μm wavelength range.

7 CHARACTERIZING HD 1160 A WITH PEPSI

In addition to characterizing HD 1160 B using the data obtained with ALES + dgvAPP360, the simultaneous high resolution PEPSI spectrum of the HD 1160 system in the optical (383–542 nm) further allows us to assess the properties of the host star HD 1160 A, which was originally classified as an A0 V star by Houk & Swift (1999). Although HD 1160 C lies at an angular separation far beyond the 2.25 arcsec diameter of the PEPSI fibre, HD 1160 B lies within this fibre diameter at a separation or ~0.78 arcsec, so the obtained PEPSI spectrum contains the spectra of both HD 1160 A and B. However, the contrast between the two is very large: 7.72 ± 0.01 mag in the 1.25 μm *J*-band, and even larger at the shorter wavelengths covered by PEPSI (Garcia et al. 2017). We therefore assumed that the contribution of HD 1160 B to the PEPSI spectrum was negligible and treated the PEPSI spectrum as solely that of HD 1160 A (see Fig. 11).

To estimate the properties of HD 1160 A, we compared the spectrum to BT-NextGen atmospheric models, which are computed with the use of the PHOENIX code (Hauschildt, Allard & Baron 1999; Allard et al. 2012). The input parameters for the model spectra were effective temperature ($T_{\rm eff}$), surface gravity (log(g)), and metallicity, the latter of which was taken as solar for HD 1160 A. The models were convolved to the resolution of the PEPSI instrument and broadened by the rotation of the star ($v \sin i$). We identified the best-fitting values for these parameters by determining the χ^2 values for a grid of models, varying $T_{\rm eff}$ (8800–9800 K in steps of 200 K),

log(g) (1.5–4.5 in steps of 0.5), and $v \sin i$ (80–120 km s^{-1} in steps of 1 km s^{-1}). The ranges of these parameters were chosen based on an initial visual inspection of the PEPSI spectrum using the digital spectral classification atlas of Gray (2000). The model grid spectra were normalized with splines fitted at similar (continuum) points for a given $T_{\rm eff}$. The same continuum points are used for a re-normalization of the PEPSI spectrum with a spline to match the normalization of the grid spectra. However, the shape of the Balmer lines appears to be inconsistent between lines, which is hard to explain with any intrinsic properties for this type of star (Gray 2000). We interpret this as a systematic error arising from residual fringing, and therefore excluded the region around the Hβ and Hγ lines from the fitting procedure. The region of the spectrum that we used for the fitting process was therefore 392–429 nm.

The errors on the PEPSI data points given by the automated pipeline are on average 0.0003 per cent of the flux, which corresponds to an extremely high S/N of $\sim 330\,000$ that we interpret as implausible since the PEPSI exposure time calculator requires ~ 1.4 yr of exposure time to achieve this, while our exposure times were $\sim 14\,800$ s. Furthermore, the spectrum seems to contain a low level sinusoidal-like structure, which most likely arises from systematics introduced by the original normalization performed by the automated pipeline. We therefore recalculated the error on each data point using the S/N instead measured from the normalized spectrum by taking the inverse of the standard deviation of the flux in the continuum, which gives S/N = ~ 500 (or ~ 0.2 per cent of the normalized flux).
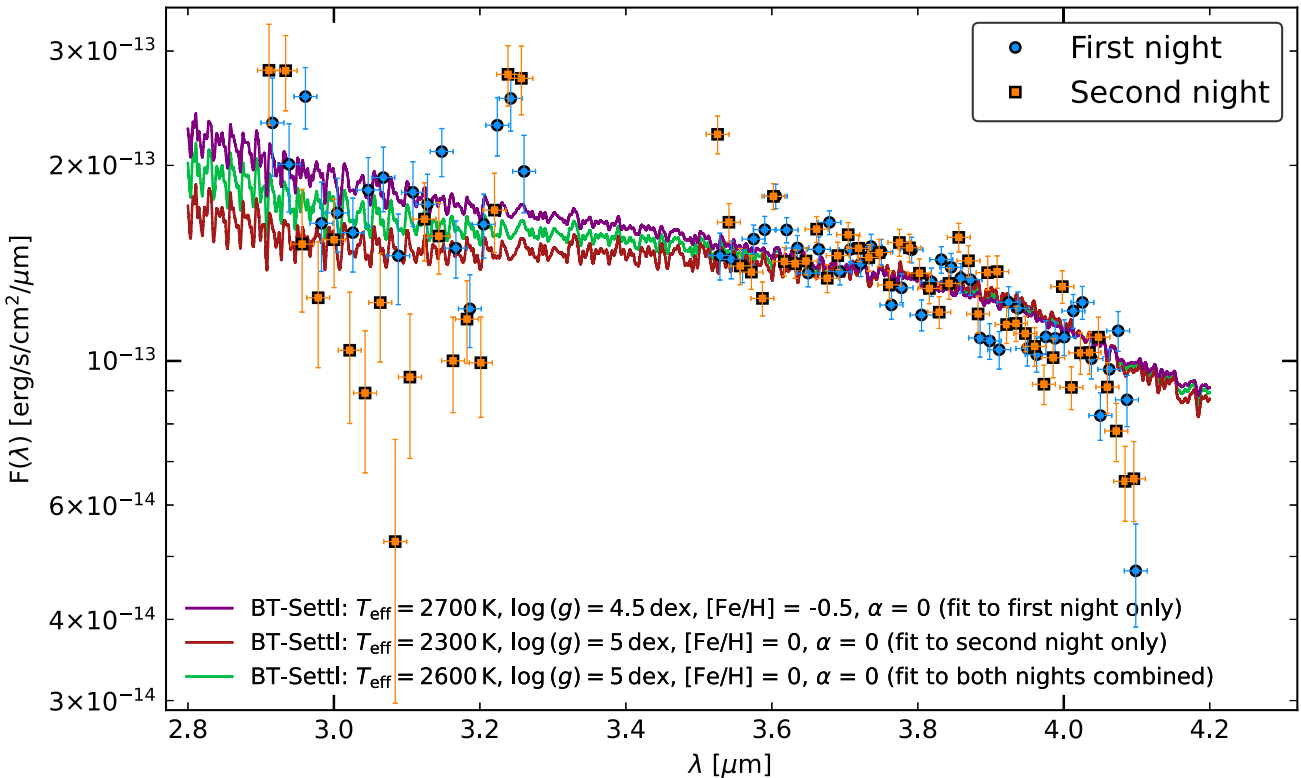
Figure 10. The best-fitting models to the flux-calibrated ALES spectrum of HD 1160 B. The large difference in the temperatures of the best-fitting models appears to arise from the difference in flux between the two nights in the 3.0–3.2 μm region. Data points in the shaded regions in Fig. 9 were not included in these fits and are therefore not shown.

Table 3. The physical properties of HD 1160 B as derived by fitting BT-Settl models to its spectrum from the first night, the second night, and both nights combined. These values are the weighted means calculated based on the χ^2 values of each model fit. The uncertainties reported here are only the statistical errors based on sided variance estimates. Where the fitting procedure tends to prefer models at the edge of the allowed parameter range, we instead report upper/lower limits. The bottom part of the table shows the estimated mass ranges for HD 1160 B and the corresponding mass ratios q relative to HD 1160 A, as found in Section 8.2.1 by evaluating BT-Settl isochrones at our luminosity values. These ranges are wide due to the wide age range considered, 10–125 Myr.

Property	First night	Second night	Both nights
$T_{\rm eff}$ (K)	2794^{+115}_{-133}	2279^{+79}_{-157}	2554^{+49}_{-93}
log(g) (dex)	≥ 4.08	≥ 4.41	≥ 4.49
Metallicity	≤ 0.27	$0.00^{+0.41}_{-0.00}$	≤ 0.05
Radius ($R_{\rm Jup}$)	$1.46^{+0.08}_{-0.06}$	$1.77^{+0.06}_{-0.05}$	$1.59^{+0.06}_{-0.03}$
log($L/L_\odot$)	$-2.91^{+0.03}_{-0.03}$	$-3.09^{+0.03}_{-0.06}$	$-2.99^{+0.02}_{-0.03}$
Mass ($M_{\rm Jup}$)	18.0–81.4	15.5–65.4	17.1–72.1
Mass ratio q	0.008–0.038	0.007–0.030	0.008–0.034

This value is then weighted by $\sqrt{F_{\rm i}}$, where $F_{\rm i}$ is the flux for a given wavelength point i, to calculate the observed errors for each wavelength point.

We found that the resulting best-fitting model, taken as that with the lowest χ^2 value (= 14.46), has $T_{\rm eff} = 9200^{+200}_{-100}$ K, $v \sin i = 96^{+6}_{-4}$ km s^{-1}, and log(g) = $3.5^{+0.5}_{-0.3}$ dex, where the errors on these values are based on the model grid spacing and distribution of χ^2 values. This

corresponds to an A1 IV-V classification for HD 1160 A (Cox 2000). This best-fitting model is shown overplotted on the PEPSI spectrum of HD 1160 A in the left panel of Fig. 11. The right panel then shows the χ^2 distribution for models with a log(g) of 3.5 over temperature and $v \sin i$. The relatively high χ^2 values, even for the best-fitting model, are due to normalization differences between the model and the spectrum, the very small errors on the flux, and the large grid separation for $T_{\rm eff}$ and log(g) for BT-Nextgen models. We discuss these results further in Section 8.3.

8 DISCUSSION

8.1 HD 1160 B light curves

8.1.1 The variability of HD 1160 B

In Section 5.4, we recovered the high-amplitude $\sim$3.2 h periodic variability signal identified by Sutlieff et al. (2023) in the first night of the detrended differential white-light curve of HD 1160 B. We also found that some data points in the light curve from our additional night deviate from equilibrium flux, albeit with a smaller amplitude. However, we do not identify any periodic signals in the light curve from this second night, nor in the full light curve covering both epochs. In both of these cases, all peaks in their respective periodograms lie well below the 1 per cent level.

Let us first consider the case that HD 1160 B is variable. There are several physical mechanisms that could potentially explain the decrease or absence of variability that we see on the second night. Variability in substellar objects arises from clouds or other atmospheric features, such as magnetic spots if the object is of higher
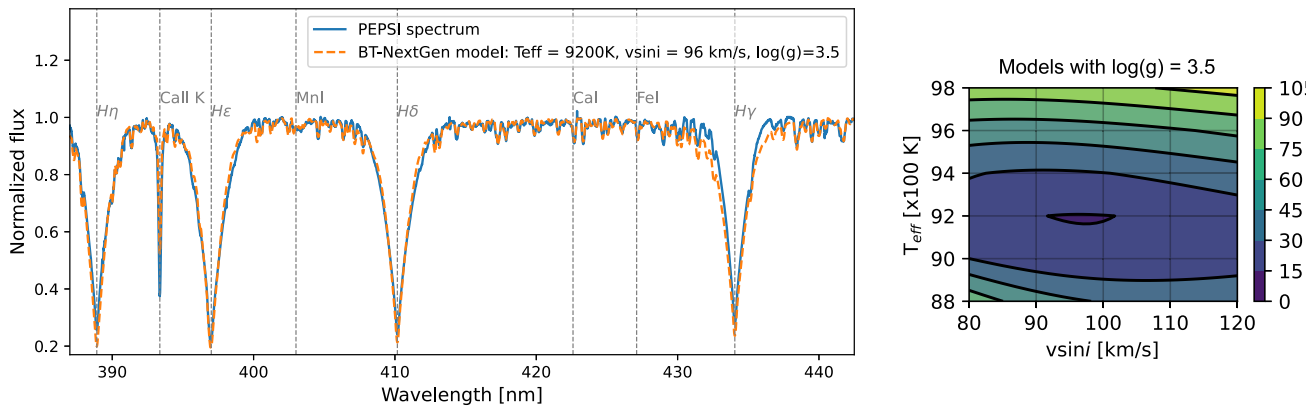
Figure 11. The left panel shows the PEPSI spectrum of the host star HD 1160 A in blue, overplotted with the best-fitting model from BT-Nextgen in orange. The fitting process was carried out for the region of the spectrum covering 392–429 nm. The contour plot in the right panel shows the χ^2 distribution for several temperatures and $v \sin i$ at fixed log(g) of 3.5.

mass, rotating in and out of view over their rotation periods (e.g. Ackerman & Marley 2001; Morales et al. 2010; Goulding et al. 2012; Radigan et al. 2014; Metchev et al. 2015; Tan & Showman 2019; Vos et al. 2022). Where multiple such features with different sizes are present in the atmosphere of a companion at different locations, the resulting variability signal can appear irregular in amplitude, phase, and/or periodicity (e.g. Tackett, Herbst & Williams 2003; Leggett et al. 2016). It is possible that we are seeing this effect in the full light curve of HD 1160 B; if its true rotation period is in fact longer than ~3.2 h (and perhaps even longer than the baseline of a single epoch), then we could be viewing it at a different phase in its rotation on the second night. In this case, additional observations would be required to cover the full rotation period of HD 1160 B and verify whether or not these trends repeat. Regardless, a ~3.2 h period is consistent with the fastest rotation periods of young isolated objects with a similar spectral type to HD 1160 B (i.e. late M- and early L-dwarfs), which have periods ranging from ~2–72 h (e.g. Bailer-Jones 2004; Popinchalk et al. 2021; Vos et al. 2022). Another possibility is that the difference in the level of variability is due to evolution in the surface features and atmospheric dynamics that cause the variability (e.g. Tan & Showman 2021). Many studies have identified changing variability in the light curves of brown dwarfs and planetary-mass objects, including both long-term trends over hundreds of rotation periods and rapid light curve evolution from one night to the next or even between consecutive rotations (e.g. Gelino et al. 2002; Artigau et al. 2009; Radigan et al. 2012; Gillon et al. 2013; Karalidi et al. 2016; Apai et al. 2017, 2021; Zhou et al. 2022; Fuda et al. 2024). If the rotation period of HD 1160 B is ~3.2 h, it would have completed ~5 rotations between the end of the observing sequence on the first night and the start of observations on the second night, which may be long enough for rapid evolution to have occurred. However, we also note that the first night covers 7.81 h which corresponds to only ~2.5 rotations of HD 1160 B. It may be the case that this is insufficient to accurately derive the rotation period of HD 1160 B. Regardless, significant night-to-night changes are especially possible if the atmosphere has a banded structure with sinusoidal surface brightness induced by planetary-scale waves, as multiple bands with slightly different periods can give rise to a beating effect. For example, Apai et al. (2017) found that an analytical model combining three sinusoids with different periods (corresponding to three atmospheric bands) produces a function that can rapidly fluctuate from low to high amplitudes. They found that this model

matches the light curve evolution in their *Hubble Space Telescope* observations of an L/T transition brown dwarf, which shows low-amplitude variability on one day and high-amplitude variability on the next in a similar manner to HD 1160 B.

Several studies exploring the variability of substellar objects in different wavebands have further found that light curves can have similar shapes at different wavelengths, but with an offset in phase as different wavelengths probe different atmospheric pressures (e.g. Buenzli et al. 2012; Biller et al. 2013, 2018; Yang et al. 2016; Ge et al. 2019; McCarthy et al. 2024; Plummer et al. 2024). Since our differential light curve of HD 1160 B is a white-light curve integrated over a wide wavelength range, such wavelength-dependent phase offsets could lead to a 'cancelling out' effect if they were of certain amplitudes. This effect could impact the light curve of HD 1160 B if its variability has different periods at different wavelengths, such that their phases mismatch at certain times.

Sutlieff et al. (2023) highlighted that if HD 1160 B is a low-mass M-dwarf, a short-lived flaring period could be the cause of its ~8.8 per cent semi-amplitude variability on the first night. If this is indeed the case for HD 1160 B, this would be consistent with both the high-amplitude variability seen on the first night and its decrease or absence on the second night. However, while flaring events of this magnitude have been observed in the infrared, they are expected to be rare (e.g. Davenport et al. 2012; Goulding et al. 2012; Tofflemire et al. 2012).

We must now also consider the possibility that one or more unknown systematics could be responsible for the high-amplitude periodic variability that we see on the first night. However, it is not clear what systematic effect could induce such high-amplitude periodic variations on one night and not do so on the following night, given that the same methodology was applied to each epoch. The observing conditions were very similar and highly stable on both nights. If we consider the decorrelation parameters used in the detrending procedure (Fig. 3), we see that the airmass, companion position, and stellar position all follow approximately the same trends on each night. This would appear to rule out residual systematics arising from these parameters as the source of the light curve differences between each night. The air temperature does differ slightly in the second half of each night but is otherwise broadly similar, and any correlation arising from this difference is unlikely to be significant enough to explain what we see, particularly after the detrending process has been applied. One possibility could be
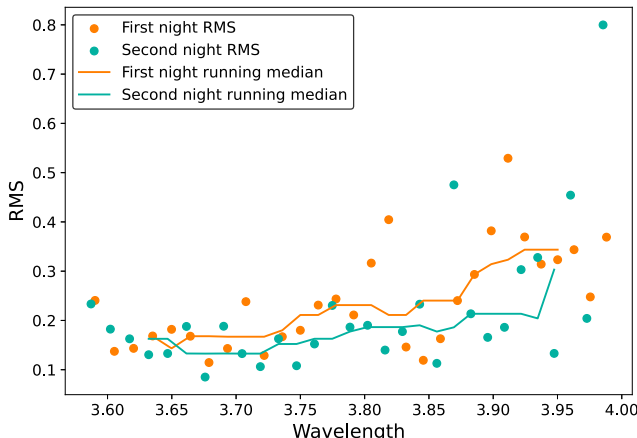
Figure 12. The RMS values, as a function of wavelength, for the 30 detrended differential light curves in the individual wavelength channels (shown in Fig. 5) that were combined to obtain the white-light curve. The binning is the same at 18 min of integration time per bin. The running medians of these values for each night are also shown, based on a window size of 7. The RMS increases with wavelength on both nights.

that there is an additional systematic connected to the flexure of the ALES lenslet array as the telescope rotates. However, any such effects should already be accounted for by the inclusion of the pixel positions of HD 1160 A and B in the detrending process. An alternative parameter probing this flexure would be the pointing altitude of the telescope, which again follows the same trend on each night (and follows an inverse relationship to airmass), suggesting that this is unlikely to be the source of the differences between the two nights. Furthermore, Sutlieff et al. (2023) found that the shape of the raw light curves is robust against issues arising from lenslet flexure by comparing data processed using wavelength calibration frames obtained at different pointing altitudes. We also note the sharp increase in flux in the raw differential light curve on the second night at ∼27 h. This feature appears to be connected to the large offset in the stellar (and companion) x-position at this time, and is accounted for in the linear regression and hence removed in the detrended light curve.

Sutlieff et al. (2023) also used the RMS values of the detrended differential light curves in each of the 30 individual wavelength channels from the first night as a metric to search for wavelength-dependent trends. To allow a comparison to their results, we repeated this for the individual channel light curves on both nights (Fig. 5). These RMS measurements are shown as a function of wavelength in Fig. 12, along with the running median on each night using a window size of 7. Sutlieff et al. (2023) identified a tentative increase in the RMS towards longer wavelengths on the first night. We see this trend again on both the first and second nights, as indicated by the upward curves of the running median. Although this trend could potentially indicate an increase in variability with wavelength, this increase in RMS is more likely explained by noise due to the higher thermal background at longer wavelengths. There are outliers from this trend, which could in principle be explained by changes in the atmosphere of the companion between nights. However, the wavelengths at which these outliers occur are not consistent between nights and as the S/N in each individual wavelength channel is not high, we do not speculate further on their origin here.

Although the nature of the variability of HD 1160 B remains unclear, the additional night of variability monitoring presented here shows that this variability does not follow a simple periodic trend and

highlights the complexities of interpreting the light curves of high-contrast substellar companions. Future ground-based observations will help to shed light on the trends in the light curves of HD 1160 B through additional epochs that provide a longer baseline when combined with our data, and the greater photometric precision provided by space-based facilities such as *JWST* could further help to constrain its variability amplitudes.

8.1.2 Precision of vAPP differential spectrophotometric monitoring

Our additional night of variability monitoring through differential spectrophotometric monitoring combined with the dgvAPP360 allows us to test whether this recently developed technique can achieve the same precision at multiple epochs. Sutlieff et al. (2023) found that this technique did not reach a systematic noise floor on the first night, suggesting that the precision would continue to improve with a longer baseline and increasing bin size. In Section 5.4, we measured the RMS as a function of bin size for the detrended differential white-light curves on each night and both nights combined (Fig. 7). As noted previously, the RMS trends for the first night and both nights combined cases do sit at a slightly higher level than on the second night, but this is expected as no astrophysical variability signal has been removed from either night and the variability is of higher amplitude on the first night. Aside from this offset, we see that the RMS follows the same trend on both nights; both decrease according to the trend of the white noise and do not plateau. This is also the case for the light curve covering both nights combined. This suggests that the data possesses similar noise properties at both epochs and therefore that the precision reached with this technique can be reliably repeated. The RMS of the detrended differential white-light curve from the second night is 0.035 in bins of 18 min, corresponding to a precision of 3.5 per cent. This is comparable to the 3.7 per cent precision measured by Sutlieff et al. (2023) for the first night light curve with the same bin size, indicating that this precision level is repeatable over multiple epochs. Since we do not appear to reach the photon noise limit with these observations, future observations may be able to achieve a greater precision by improving the process used to detrend the differential light curve of the companion. This could be done by adapting more complex approaches used for exoplanet transmission spectroscopy studies, including techniques using Gaussian processes which do not assume that the systematics have any particular dependence on the telluric/instrumental parameters (e.g. Gibson et al. 2012; Evans et al. 2013; Nikolov et al. 2018; Carter et al. 2020; Diamond-Lowe et al. 2020a,b; Panwar et al. 2022a; Aigrain & Foreman-Mackey 2023). However, we note that robustly assessing the true deviation of these trends from the white noise model is difficult due to the possible astrophysical variability. Furthermore, although such techniques will help to minimize the risk of overfitting, transmission spectroscopy targets are typically pixel-stabilized. Thus, implementing them for non-stabilized differential spectrophotometry targets will require careful consideration.

8.2 Spectral characterization of HD 1160 B

In Section 6.1, we presented the extracted spectra of HD 1160 B for each night and noted an offset in the spectra of HD 1160 B from each night in the 3–3.2 μm wavelength region, where the data points from the second night appear to lie slightly lower than those from the first night. The cause of this offset is unclear. The time-averaged flux measurements of the host star HD 1160 A on each night are

consistent across all wavelengths, indicating that this is not caused by throughput differences arising from differences in the weather conditions between the two nights. A possibility is that this feature is astrophysical and arises from the intrinsic variability of HD 1160 B, with it appearing fainter in this wavelength region on the second night. In addition to this feature, the scatter of the data points at longer wavelengths (e.g. 3.6–4.0 μm) is also larger than would be expected from the fitted models. If our uncertainties are correctly estimated, then this may also be due to the effects of variability; a greater scatter in the spectrum of HD 1160 B would be expected if its variability has different properties at different wavelengths. However, we cannot rule out that this scatter is a systematic effect.

Regardless of the origin of the offset at 3–3.2 μm, it has a significant impact on the results of the atmospheric model fitting described in Section 6.2. This process produced significantly different values for the physical properties of HD 1160 B depending on whether the models were fit to the spectra from the first night alone, the second night alone, or both nights combined (Table 3). The values for effective temperature T_{eff} cover a particularly large range, from 2279^{+79}_{-157} K for the fit to the second night to 2794^{+115}_{-133} K on the first night (a $>1\sigma$ difference). The effective temperatures derived from the second night and both nights combined spectra are much cooler than those in the literature, but the higher temperature from the first night is consistent with previous measurements to within 1σ. Maire et al. (2016) determined a T_{eff} for HD 1160 B of 3000 ± 100 K through atmospheric modelling, consistent with the 3000–3100 K value found by Garcia et al. (2017), although the latter study noted that they could not rule out slightly cooler temperatures. Our value derived from the spectrum from the first night also overlaps with the 2800–2900 K range estimated by Mesa et al. (2020).

All three of our constraints for surface gravity log(g) are consistent with the 4.0–4.5 dex range estimated by Garcia et al. (2017) (who also could not rule out slightly higher values), and consistent within 2σ with Mesa et al. (2020), who estimated a lower log(g) of 3.5–4.0 dex. Maire et al. (2016) were not able to constrain the surface gravity in their study. However, we note that surface gravity is not strongly constrained by our atmospheric model fitting. Our inferred radii from the fits to the first night and both nights spectra are consistent with the 1.55 ± 0.1 R_{Jup} radius inferred by Garcia et al. (2017), but our radius for the second night spectrum is slightly larger. Finally, all three of our inferred luminosities log(L/L⊙) are lower than the -2.76 ± 0.05 dex value measured by Garcia et al. (2017). However, our luminosity from the first night is consistent within 1σ with that found by Maire et al. (2016), log(L/L⊙) $= -2.81 \pm 0.10$ dex.

If we consider these results in full, the spectrum of HD 1160 B on our second night of observations does not appear to be consistent with the literature. If the differences between the spectra from each night at bluer wavelengths are due to astrophysical variability in the atmosphere of HD 1160 B, this highlights the impact that this can have on the results of fitting models to the atmospheres of substellar companions. Difficulties in fitting the spectrum of HD 1160 B have also been noted previously. When analysing the SPHERE spectra in the *Y*, *J*, and *H* bands, Mesa et al. (2020) found that HD 1160 B has a spectrum that is not well matched by any spectra in current spectral libraries, and were only able to obtain good fits by considering the *Y*+*J* and *H* bands separately. Several studies of other substellar companions have also reported such issues when trying to fit their spectra, sometimes finding wide-ranging results depending on the wavebands considered (e.g. Stone et al. 2020; Sutlieff et al. 2021; Ward-Duong et al. 2021; Whiteford et al. 2023; Phillips, Liu & Zhang 2024).

Simultaneous observations over a broad wavelength range with facilities such as *JWST* may help to explain these discrepancies between wavebands and further identify whether the differences in the spectrum of HD 1160 B between epochs are due to time variability (Hinkley et al. 2022; Kammerer et al. 2022; Carter et al. 2023; Miles et al. 2023; Rigby et al. 2023; Manjavacas et al. 2024; Petrus et al. 2024). Ground-based high-resolution spectroscopy may further help us to determine its nature by resolving specific molecular lines that constrain effective temperature, surface gravity, and other physical properties (e.g. Birkby et al. 2013; Birkby 2018; Hoeijmakers et al. 2018; Brogi & Line 2019; van Sluijs et al. 2023). High-resolution spectroscopy could also measure the $v \sin i$ of HD 1160 B, which would provide an independent and complementary upper limit of its rotation period (e.g. Snellen et al. 2014; Schwarz et al. 2016; Bryan et al. 2018, 2020; Wang et al. 2021b; Xuan et al. 2022; Palma-Bifani et al. 2023; Landman et al. 2024; Parker et al. 2024).

8.2.1 The mass of HD 1160 B

It is further possible to infer estimates for the mass of HD 1160 B using our luminosity estimates from Section 6.2 and values for the age of the HD 1160 system. We used the BT-Settl (Allard 2014; Baraffe et al. 2015) isochrones for this purpose, which are valid for brown dwarfs and low mass stars. To obtain mass estimates, we first interpolated over the model grid of each isochrone and then evaluated them at our luminosity values. As the resulting mass estimates are highly age-dependent and the age of the HD 1160 system is not well constrained, we carefully considered the range of age estimates in the literature and chose to use a 10–125 Myr range. This is a combination of the 20–125 Myr age range found by Garcia et al. (2017) considering the properties of HD 1160 A and a range of evolutionary models, and the lower 10–20 Myr ages favoured by the results of Mesa et al. (2020) (the former study also produced a range based on HD 1160 ABC together, but this was narrower 80–125 Myr). Our chosen range also covers the $\sim$120 Myr age that the HD 1160 system would be expected to have if it is a member of the Psc-Eri stellar stream, as suggested by Curtis et al. (2019). Maire et al. (2016) did allow ages up to 300 Myr in their study, but ages this old appear to be ruled out by Garcia et al. (2017).

The resulting estimated mass ranges are shown in Table 3. We also include the corresponding values for the mass ratio relative to HD 1160 A, *q*, assuming a stellar mass of 2.05 M⊙ (A1 V; Pecaut & Mamajek 2013). Older ages return higher mass values, and vice versa. Our full range of mass estimates covers 16–81 M_{Jup}. This places HD 1160 B comfortably above the deuterium burning limit ($\sim$11-16.3 M_{Jup}; Spiegel, Burrows & Milsom 2011), but does not rule out the possibility that it is a low mass star above the hydrogen burning limit (78.5 M_{Jup}; Chabrier et al. 2023). This is fully consistent with mass estimates in the literature, as we might expect given the broad age range assumed. Nielsen et al. (2012) estimated the mass of HD 1160 B to be 33^{+12}_{-9} M_{Jup} upon its discovery, and Maire et al. (2016) found a mass range of 39–166 M_{Jup} based on their wider range of allowable system ages. Garcia et al. (2017) later found a mass range of 35–90 M_{Jup}. Finally, Mesa et al. (2020) estimated a mass of $\sim$20 M_{Jup} for HD 1160 B, which falls at the lower end of our range.

Our ability to precisely estimate the mass of HD 1160 B is severely limited by the highly uncertain age of the HD 1160 system, thus it will be difficult to further constrain the mass of this companion without either tighter constraints on its age or a dynamical mass measurement (e.g. Konopacky et al. 2010; Crepp et al. 2012; Dupuy et al. 2016; Dupuy & Liu 2017; Brandt, Dupuy & Bowler 2019; Biller et al. 2022; Rickman et al. 2022).

8.3 PEPSI characterization of HD 1160 A

In Section 7, we fitted BT-NextGen models to the PEPSI data of HD 1160 A and estimated its physical properties, finding $T_{\rm eff}$ = 9200^{+200}_{-100} K, $v\sin i = 96^{+6}_{-4}$ km s^{-1}, and $\log(g) = 3.5^{+0.5}_{-0.3}$ dex. If we compare these physical properties to those of the best-fitting model found by using VOSA to fit the literature SED of HD 1160 A for the flux calibration process in Section 6.1, the temperature and metallicity have the same values but the surface gravity here is lower than that of the $\log(g) = 4.5$ dex model found with VOSA. This difference in surface gravity does not significantly impact the flux calibration of the spectra of HD 1160 B in Section 6.1, as the best-fitting model found with VOSA is convolved to the $R \sim 40$ resolution of ALES prior to being used for this purpose. At this resolution, the two stellar models are indistinguishable and do not lead to differences in the HD 1160 B spectral fitting results.

If we assume the BT-Settl model grid spacing for $\log(g)$, 0.5 dex, as the uncertainty on the VOSA result, the two values are consistent within 1σ. We note that surface gravity is difficult to constrain with atmospheric models, and similarly good fits to the PEPSI data could also be obtained with slightly higher surface gravities. However, if HD 1160 A does have $\log(g) = 3.5$, this may be an indicator of youth, as older objects are likely to have higher surface gravities (e.g. Baraffe et al. 2015).

Our measurement of $v\sin i = 96^{+6}_{-4}$ km s^{-1} is fully consistent with those previously found by Bowler et al. (2023), who measured the $v\sin i$ of HD 1160 A at three different epochs using the Tull Coudé Spectrograph on the Harlan J. Smith telescope, finding values of $v\sin i = 96 \pm 10$, 97 ± 7, and 95 ± 7 km s^{-1} at each epoch, respectively.

Our derived values for the physical properties of HD 1160 A from the PEPSI spectrum correspond to an A1 IV-V spectral type. This is a slightly later spectral type than the A0 V classification found by Houk & Swift (1999) using photographic plates. Nielsen et al. (2012) previously noted that HD 1160 A is underluminous for its position on the HR diagram, based on it being an A0 V star, and interpreted this as a sign of youth (e.g. Jura et al. 1998). However, if HD 1160 A is an A1 V star, this may partially account for this apparent underluminosity. As we also measured the $v\sin i$ of HD 1160 A, we further considered the alternative possibility that gravity darkening could help to explain this. If a star rotates rapidly it becomes oblate, leading to a greater radius and hence lower temperature and brightness at its equator compared to its poles (Monnier et al. 2007; Espinosa Lara & Rieutord 2011; Lipatov, Brandt & Batalha 2022). The orbital inclination of HD 1160 B is almost edge-on ($92^{+8.7}_{-9.3}$°; Bowler et al. 2020a). Assuming that the stellar rotation axis of HD 1160 A is aligned with the orbit of HD 1160 B, rapid rotation would therefore lead to an apparent decrease in its luminosity as viewed from Earth. However, a typical A-type star has a much faster rotation (e.g. ~190 km s^{-1} for an A0 star) than our rotational velocity measurement $v\sin i = 96^{+6}_{-4}$ km s^{-1} (McNally 1965; Nielsen et al. 2013). Thus, gravity darkening caused by rapid rotation cannot be the underlying cause of the underluminosity, if HD 1160 A is viewed approximately edge-on. If HD 1160 A is instead viewed pole-on (i.e. $i \sim 0$), its true rotational velocity v would be far faster and therefore lead it to appear brighter at its poles than its equator and hence to a relative increase in its luminosity as viewed from Earth. This indicates that gravitational darkening cannot explain any underluminosity of HD 1160 A, and that this is better accounted for by it being of a later spectral type than previously thought.

9 CONCLUSIONS

We present here a new study of the HD 1160 system using two nights of observations obtained with the Large Binocular Telescope. This work is divided into three parts: variability monitoring of red companion HD 1160 B with the dgvAPP360 coronagraph and the ALES IFS; a $R \sim 40$ spectral characterization of HD 1160 B using the same data; and lastly a spectral characterization of host star HD 1160 A using $R = 50\,000$ high resolution spectroscopy obtained with the PEPSI spectrograph.

The variability analysis of HD 1160 B was conducted following the technique of gvAPP-enabled differential spectrophotometric monitoring recently presented by Sutlieff et al. (2023), who demonstrated this approach with the first night of observations used here. We first processed the LBT/ALES + dgvAPP360 data and extracted aperture photometry of both HD 1160 A and B, before combining the data in the wavelength dimension and dividing the companion flux by that of the star to produce a differential white-light curve for HD 1160 B spanning both nights. We then further detrended the light curve using a multiple linear regression approach. We find that we recover the high-amplitude ~3.2 h periodic variability identified by Sutlieff et al. (2023) in the first night, but that the second night light curve does not contain significant periodic variability, potentially indicating rapid time evolution in the atmosphere of HD 1160 B and highlighting the complexity of interpreting the light curves of high-contrast substellar companions. We also analysed the precision achieved in the detrended differential white-light curve on each night and found that the noise properties were similar. This suggests that gvAPP-enabled differential spectrophotometric monitoring achieves a repeatable precision at the few per cent level over multiple epochs and that we do not reach the photon noise limit. Thus, a greater precision could be achieved in future studies if residual systematics in the differential light curves can be further mitigated using more advanced detrending approaches such as those using Gaussian processes (e.g. Gibson et al. 2012; Panwar et al. 2022a).

We conducted our spectral characterization of HD 1160 B by instead combining the LBT/ALES + dgvAPP360 observations over the time sequence for each night, thereby producing 2.9–4.1 μm spectra of the companion. These spectra are the first for this target in the mid-infrared and are therefore highly complementary to previous studies in the literature. We find that the spectrum of HD 1160 B from the second night is systematically fainter in the 3.0–3.2 μm wavelength range than on the first night, which could be due to the intrinsic variability of the companion if this difference is astrophysical. We then fit these spectra with BT-Settl atmospheric models, considering each night separately and both nights together, and found that the results differ considerably depending on the data being fitted. Our effective temperature $T_{\rm eff}$ estimates range from 2279^{+79}_{-157} K for the second night spectrum to 2794^{+115}_{-133} K on the first night. This first night $T_{\rm eff}$ is consistent with the literature, but those derived from the second night and both nights combined spectra are cooler. Our inferred luminosities are lower than those in the literature, but our radius estimates are mostly consistent. Overall, we conclude that the spectrum of HD 1160 B on the second night of our observations is not consistent with the literature. The differences in the results obtained for each spectrum highlights the impact that variability can have on atmospheric model fitting for substellar companions. Simultaneous observations over a broad wavelength range with facilities such as *JWST* may help to resolve the ambiguities arising from these model fits and determine whether the differences

2186 *B. J. Sutlieff et al.*

in the spectrum of HD 1160 B between epochs are due to time variability.

By evaluating our luminosity estimates with BT-Settl isochrones over an age range of 10–125 Myr, we also estimated the mass of HD 1160 B. We report a 16–81 $M_{\rm Jup}$ mass range, consistent with previous estimates in the literature. This places HD 1160 B comfortably above the deuterium burning limit, but also allows the possibility that it is a low mass star above the hydrogen burning limit.

Lastly, we performed a new characterization of host star HD 1160 A by comparing the $R \sim 50\,000$ high resolution spectrum obtained with PEPSI to BT-NextGen atmospheric models. We found values for the physical properties of HD 1160 A; $T_{\rm eff} = 9200^{+200}_{-100}$ K, log(g) $= 3.5^{+0.5}_{-0.3}$, and $v \sin i = 96^{+6}_{-4}$ km s^{-1}. This model corresponds to a spectral type of A1 IV-V, which is slightly later than the literature A0 V classification found by Houk & Swift (1999) using photographic plates. This may explain the apparent underluminosity of HD 1160 A previously noted by Nielsen et al. (2012). By considering our rotational velocity $v \sin i$ measurement alongside the known near edge-on inclination angle of the HD 1160 system, we find that HD 1160 A rotates slower than the typical A-type star, and hence rule out gravitational darkening as the cause of any underluminosity.

Tighter limits on the age of the HD 1160 system or dynamical mass measurements of each component are key if the physical properties of HD 1160 A and B are to be constrained further. Observations over a broad wavelength range or at a high spectral resolution will also help to resolve the ambiguities in the spectrum of HD 1160 B, while additional epochs of ground-based differential spectrophotometric monitoring or high-precision space-based monitoring will shed light on its variability.

DATA AVAILABILITY

The data from the LBT/ALES + dgvAPP360 and LBT/PEPSI observations underlying this article will be available in the Research Data Management Zenodo repository of the Anton Pannekoek Institute for Astronomy shortly after publication, at https://doi.org/10.5281/zenodo.7051242.

REFERENCES

Ackerman A. S., Marley M. S., 2001, ApJ, 556, 872
Aigrain S., Foreman-Mackey D., 2023, ARA&A, 61, 329

---

[2] http://whereistheplanet.com/
[3] Python Software Foundation; https://www.python.org/

Allard F., 2014, in Booth M., Matthews B. C., Graham J. R., eds, Proc. IAU Symp. 299, Exploring the Formation and Evolution of Planetary Systems. Cambridge Univ. Press, Cambridge, p. 271

Allard F., Homeier D., Freytag B., 2011, in Johns-Krull C., Browning M. K., West A. A., eds, ASP Conf. Ser. Vol. 448, 16th Cambridge Workshop on Cool Stars, Stellar Systems, and the Sun. Astron. Soc. Pac., San Francisco, p. 91

Allard F., Homeier D., Freytag B., 2012, Phil. Trans. R. Soc. Lond. Ser. A, 370, 2765

Allard F., Homeier D., Freytag B., Schaffenberger W., Rajpurohit A. S., 2013, Mem. Soc. Astron. Ital. Suppl., 24, 128

Amara A., Quanz S. P., 2012, MNRAS, 427, 948

Apai D. et al., 2016, ApJ, 820, 40

Apai D. et al., 2017, Science, 357, 683

Apai D., Nardiello D., Bedin L. R., 2021, ApJ, 906, 64

Arcangeli J., Désert J. M., Parmentier V., Tsai S. M., Stevenson K. B., 2021, A&A, 646, A94

Artigau É., Bouchard S., Doyon R., Lafrenière D., 2009, ApJ, 701, 1534

Ashraf A., Bardalez Gagliuffi D. C., Manjavacas E., Vos J. M., Mechmann C., Faherty J. K., 2022, ApJ, 934, 178

Astropy Collaboration 2013, A&A, 558, A33

Astropy Collaboration 2018, AJ, 156, 123

Astropy Collaboration 2022, ApJ, 935, 167

Bailer-Jones C. A. L., 2004, A&A, 419, 703

Bailey V. et al., 2014a, ApJ, 780, L4

Bailey V. P. et al., 2014b, in Marchetti E., Close L. M., Vran J.-P., eds, Proc. SPIE Conf. Ser. Vol. 9148, Adaptive Optics Systems IV. SPIE, Bellingham, p. 914803

Baraffe I., Homeier D., Allard F., Chabrier G., 2015, A&A, 577, A42

Bayo A., Rodrigo C., Barrado Y Navascués D., Solano E., Gutiérrez R., Morales-Calderón M., Allard F., 2008, A&A, 492, 277

Beuzit J. L. et al., 2019, A&A, 631, A155

Biller B. A. et al., 2010, ApJ, 720, L82

Biller B. A. et al., 2013, ApJ, 778, L10

Biller B. A. et al., 2018, AJ, 155, 95

Biller B. A. et al., 2021, MNRAS, 503, 743

Biller B. A. et al., 2022, A&A, 658, A145

Birkby J. L., 2018, preprint (arXiv:1806.04617)

Birkby J. L., de Kok R. J., Brogi M., de Mooij E. J. W., Schwarz H., Albrecht S., Snellen I. A. G., 2013, MNRAS, 436, L35

Bohn A. J. et al., 2020a, MNRAS, 492, 431

Bohn A. J. et al., 2020b, ApJ, 898, L16

Bohn A. J. et al., 2021, A&A, 648, A73

Bonavita M. et al., 2022, MNRAS, 513, 5588

Bowler B. P. et al., 2017, AJ, 153, 18

Bowler B. P., Blunt S. C., Nielsen E. L., 2020a, AJ, 159, 63

Bowler B. P., Zhou Y., Morley C. V., Kataria T., Bryan M. L., Benneke B., Batygin K., 2020b, ApJ, 893, L30

Bowler B. P. et al., 2023, AJ, 165, 164

Bradley L. et al., 2022, astropy/photutils: Zenodo (online)

Brandt T. D., Dupuy T. J., Bowler B. P., 2019, AJ, 158, 140

Briesemeister Z. et al., 2018, in Evans C. J., Simard L., Takami H., eds, Proc. SPIE Conf. Ser. Vol. 10702, Ground-based and Airborne Instrumentation for Astronomy VII. SPIE, Bellingham, p. 107022Q

Briesemeister Z. W. et al., 2019, AJ, 157, 244

Broeg C., Fernández M., Neuhäuser R., 2005, Astron. Nachr., 326, 134

Brogi M., Line M. R., 2019, AJ, 157, 114

Bryan M. L., Benneke B., Knutson H. A., Batygin K., Bowler B. P., 2018, Nat. Astron., 2, 138

Bryan M. L., Ginzburg S., Chiang E., Morley C., Bowler B. P., Xuan J. W., Knutson H. A., 2020, ApJ, 905, 37

Buenzli E. et al., 2012, ApJ, 760, L31

Burgasser A. J., Cruz K. L., Cushing M., Gelino C. R., Looper D. L., Faherty J. K., Kirkpatrick J. D., Reid I. N., 2010a, ApJ, 710, 1142

Burgasser A. J. et al., 2010b, ApJ, 725, 1405

Carter A. L. et al., 2020, MNRAS, 494, 5449

Carter A. L. et al., 2023, ApJ, 951, L20

Chabrier G., Baraffe I., Phillips M., Debras F., 2023, A&A, 671, A119

Cox A. N., 2000, Allen's Astrophysical Quantities. Springer, New York, NY

Crepp J. R. et al., 2012, ApJ, 751, 97

Crossfield I. J. M. et al., 2014, Nature, 505, 654

Currie T. et al., 2022, Nat. Astron., 6, 751

Currie T. et al., 2023, Science, 380, 198

Curtis J. L., Agüeros M. A., Mamajek E. E., Wright J. T., Cummings J. D., 2019, AJ, 158, 77

Cutri R. M. et al., 2003, VizieR Online Data Catalog. p. II/246, Available at http://irsa.ipac.caltech.edu/applications/Gator/

Czesla S., Schröter S., Schneider C. P., Huber K. F., Pfeifer F., Andreasen D. T., Zechmeister M., 2019, PyA: Python astronomy-related packages, record ascl:1906.010

Davenport J. R. A., Becker A. C., Kowalski A. F., Hawley S. L., Schmidt S. J., Hilton E. J., Sesar B., Cutri R., 2012, ApJ, 748, 58

de Mooij E. J. W., Brogi M., de Kok R. J., Snellen I. A. G., Kenworthy M. A., Karjalainen R., 2013, A&A, 550, A54

Defrère D. et al., 2015, in Shaklan S., ed., Proc. SPIE Conf. Ser. Vol. 9605, Techniques and Instrumentation for Detection of Exoplanets VII. SPIE, Bellingham, p. 96051G

Diamond-Lowe H., Berta-Thompson Z., Charbonneau D., Kempton E. M. R., 2018, AJ, 156, 42

Diamond-Lowe H., Berta-Thompson Z., Charbonneau D., Dittmann J., Kempton E. M. R., 2020a, AJ, 160, 27

Diamond-Lowe H., Charbonneau D., Malik M., Kempton E. M. R., Beletsky Y., 2020b, AJ, 160, 188

Diamond-Lowe H., Mendonça J. M., Charbonneau D., Buchhave L. A., 2023, AJ, 165, 169

Dias W. S., Alessi B. S., Moitinho A., Lépine J. R. D., 2002, A&A, 389, 871

Doelman D. S., Snik F., Warriner N. Z., Escuti M. J., 2017, in Shaklan S., ed., Proc. SPIE Conf. Ser. Vol. 10400, Techniques and Instrumentation for Detection of Exoplanets VIII. SPIE, Bellingham, p. 104000U

Doelman D. S., Por E. H., Ruane G., Escuti M. J., Snik F., 2020, PASP, 132, 045002

Doelman D. S. et al., 2021, Appl. Opt., 60, D52

Doelman D. S. et al., 2022, AJ, 163, 217

Dupuy T. J., Kraus A. L., 2013, Science, 341, 1492

Dupuy T. J., Liu M. C., 2017, ApJS, 231, 15

Dupuy T. J., Forbrich J., Rizzuto A., Mann A. W., Aller K., Liu M. C., Kraus A. L., Berger E., 2016, ApJ, 827, 23

Ertel S. et al., 2020, in Tuthill P. G., Mérand A., Sallum S., eds, Proc. SPIE Conf. Ser. Vol. 11446, Optical and Infrared Interferometry and Imaging VII. SPIE, Bellingham, p. 1144607

Espinosa Lara F., Rieutord M., 2011, A&A, 533, A43

Evans T. M. et al., 2013, ApJ, 772, L16

Faherty J. K., Cruz K. L., Rice E. L., Riedel A., 2013, Mem. Soc. Astron. Italiana, 84, 955

Faherty J. K. et al., 2016, ApJS, 225, 10

Fitzpatrick E. L., 1999, PASP, 111, 63

Franson K. et al., 2023, AJ, 165, 39

Fuda N., Apai D., Nardiello D., Tan X., Karalidi T., Bedin L. R., 2024, ApJ, 965, 182

Fuhrmeister B. et al., 2019, A&A, 623, A24

Gaia Collaboration 2016, A&A, 595, A1

Gaia Collaboration 2023, A&A, 674, A1

Garcia E. V. et al., 2017, ApJ, 834, 162

Ge H. et al., 2019, AJ, 157, 89

Gelino C. R., Marley M. S., Holtzman J. A., Ackerman A. S., Lodders K., 2002, ApJ, 577, 433

Gibson N. P., Aigrain S., Roberts S., Evans T. M., Osborne M., Pont F., 2012, MNRAS, 419, 2683

Gillon M., Triaud A. H. M. J., Jehin E., Delrez L., Opitom C., Magain P., Lendl M., Queloz D., 2013, A&A, 555, L5

Goulding N. T. et al., 2012, MNRAS, 427, 3358

Gray R., 2000, A Digital Spectral Classification Atlas. Appalachian State University, Boone, North Carolina

Greco J. P., Brandt T. D., 2016, ApJ, 833, 134

Haffert S. Y., Bohn A. J., de Boer J., Snellen I. A. G., Brinchmann J., Girard J. H., Keller C. U., Bacon R., 2019, Nat. Astron., 3, 749

Harris C. R. et al., 2020, Nature, 585, 357

Hauschildt P. H., Allard F., Baron E., 1999, ApJ, 512, 377

Helling C., Casewell S., 2014, A&AR, 22, 80

Hinkley S. et al., 2022, PASP, 134, 095003

Hinkley S. et al., 2023, A&A, 671, L5

Hinz P. et al., 2012, in Delplancke F., Rajagopal J. K., Malbet F., eds, Proc. SPIE Conf. Ser. Vol. 8445, Optical and Infrared Interferometry III. SPIE, Bellingham, p. 84450U

Hinz P. M. et al., 2016, in Malbet F., Creech-Eakman M. J., Tuthill P. G., eds, Proc. SPIE Conf. Ser. Vol. 9907, Optical and Infrared Interferometry and Imaging V. SPIE, Belligham, p. 990704

Hinz P. M., Skemer A., Stone J., Montoya O. M., Durney O., 2018, in Evans C. J., Simard L., Takami H., eds, Proc. SPIE Conf. Ser. Vol. 10702, Ground-based and Airborne Instrumentation for Astronomy VII. SPIE, Bellingham, p. 107023L

Hoeijmakers H. J., Schwarz H., Snellen I. A. G., de Kok R. J., Bonnefoy M., Chauvin G., Lagrange A. M., Girard J. H., 2018, A&A, 617, A144

Høg E. et al., 2000a, A&A, 355, L27

Høg E. et al., 2000b, A&A, 357, 367

Hood C. E. et al., 2024, preprint (arXiv:2402.05345)

Horne K., 1986, PASP, 98, 609

Horne J. H., Baliunas S. L., 1986, ApJ, 302, 757

Houk N., Swift C., 1999, Michigan Catalogue of Two-Dimensional Spectral Types for the HD Stars; Vol. 5. Department of Astronomy, University of Michigan, Ann Arbor

Hunter J. D., 2007, Comput. Sci. Eng., 9, 90

Ilyin I. V., 2000, PhD thesis, University of Oulu, Division of Astronomy

Indebetouw R. et al., 2005, ApJ, 619, 931

Jovanovic N. et al., 2015a, PASP, 127, 890

Jovanovic N., Guyon O., Martinache F., Pathak P., Hagelberg J., Kudo T., 2015b, ApJ, 813, L24

Joye W. A., Mandel E., 2003, in Payne H. E., Jedrzejewski R. I., Hook R. N., eds, ASP Conf. Ser. Vol. 295, Astronomical Data Analysis Software and Systems XII. Astron. Soc. Pac., San Francisco, p. 489

Jura M., Malkan M., White R., Telesco C., Pina R., Fisher R. S., 1998, ApJ, 505, 897

Kammerer J. et al., 2022, in Coyle L. E., Matsuura S., Perrin M. D., eds, Proc. SPIE Conf. Ser. Vol. 12180, Space Telescopes and Instrumentation 2022: Optical, Infrared, and Millimeter Wave. SPIE, Bellingham, p. 121803N

Karalidi T., Apai D., Marley M. S., Buenzli E., 2016, ApJ, 825, 90

Keles E. et al., 2022, MNRAS, 513, 1544

Keppler M. et al., 2018, A&A, 617, A44

Kipping D., Bakos G., 2011, ApJ, 733, 36

Konopacky Q. M., Ghez A. M., Barman T. S., Rice E. L., Bailey J. I. III, White R. J., McLean I. S., Duchêne G., 2010, ApJ, 711, 1087

Konopacky Q. M. et al., 2016, ApJ, 829, L4

Kostov V., Apai D., 2013, ApJ, 762, 47

Kuzuhara M. et al., 2022, ApJ, 934, L18

Landman R. et al., 2024, A&A, 682, A48

Leggett S. K. et al., 2003, MNRAS, 345, 144

Leggett S. K. et al., 2016, ApJ, 830, 141

Leisenring J. M. et al., 2012, in McLean I. S., Ramsay S. K., Takami H., eds, Proc. SPIE Conf. Ser. Vol. 8446, Ground-based and Airborne Instrumentation for Astronomy IV. SPIE, Bellingham, p. 84464F

Lew B. W. P. et al., 2020, AJ, 159, 125

Lew B. W. P. et al., 2024, AJ, 167, 237

Li Y. et al., 2023, MNRAS, 522, 5622

Lipatov M., Brandt T. D., Batalha N. E., 2022, MNRAS, 517, 2942

Liu M. C. et al., 2010, in Ellerbroek B. L., Hart M., Hubin N., Wizinowich P. L., eds, Proc. SPIE Conf. Ser. Vol. 7736, Adaptive Optics Systems II. SPIE, Bellingham, p. 77361K

Liu P. et al., 2023, A&A, 674, A115

Liu P. et al., 2024, MNRAS, 527, 6624

Lomb N. R., 1976, Ap&SS, 39, 447

Macintosh B. et al., 2014, Proc. Natl. Acade. Sci., 111, 12661

Maire A. L. et al., 2016, A&A, 587, A56

Manjavacas E. et al., 2019, ApJ, 875, L15

Manjavacas E., Karalidi T., Vos J. M., Biller B. A., Lew B. W. P., 2021, AJ, 162, 179

Manjavacas E., Karalidi T., Tan X., Vos J. M., Lew B. W. P., Biller B. A., Oliveros-Gómez N., 2022, AJ, 164, 65

Manjavacas E., Miles-Páez P. A., Karalidi T., Vos J. M., Galloway M. L., Girard J. H., 2023, AJ, 165, 181

Manjavacas E. et al., 2024, AJ, 167, 168

Marois C., Lafrenière D., Doyon R., Macintosh B., Nadeau D., 2006, ApJ, 641, 556

Marois C., Zuckerman B., Konopacky Q. M., Macintosh B., Barman T., 2010, Nature, 468, 1080

Mawet D. et al., 2012, in Clampin M. C., Fazio G. G., MacEwen H. A., Oschmann J. M., Jr, eds, Proc. SPIE Conf. Ser. Vol. 8442, Space Telescopes and Instrumentation 2012: Optical, Infrared, and Millimeter Wave. SPIE, Bellingham, p. 844204

Mawet D. et al., 2015, ApJ, 811, 103

McCarthy A. M. et al., 2024, ApJ, 965, 83

McKinney W., 2010, in van der Walt S., Millman J., eds, Proceedings of the 9th Python in Science Conference. SciPy, Austin, Texas, p. 56

McNally D., 1965, The Observatory, 85, 166

Meingast S., Alves J., Fürnkranz V., 2019, A&A, 622, L13

Mesa D. et al., 2020, MNRAS, 495, 4279

Metchev S. A. et al., 2015, ApJ, 799, 154

Miles-Páez P. A., 2021, A&A, 651, L7

Miles-Páez P. A. et al., 2019, ApJ, 883, 181

Miles B. E. et al., 2023, ApJ, 946, L6

Milli J. et al., 2017, A&A, 597, L2

Monnier J. D. et al., 2007, Science, 317, 342

Morales J. C., Gallardo J., Ribas I., Jordi C., Baraffe I., Chabrier G., 2010, ApJ, 718, 502

Morley C. V. et al., 2018, ApJ, 858, 97

Nielsen E. L. et al., 2012, ApJ, 750, 53

Nielsen M. B., Gizon L., Schunker H., Karoff C., 2013, A&A, 557, L10

Nikolov N. et al., 2018, Nature, 557, 526

Ochsenbein F., Bauer P., Marcout J., 2000, A&AS, 143, 23

Otten G. P. P. L., Snik F., Kenworthy M. A., Miskiewicz M. N., Escuti M. J., 2014, Opt. Express, 22, 30287

Otten G. P. P. L. et al., 2017, ApJ, 834, 175

Palma-Bifani P. et al., 2023, A&A, 670, A90

Panwar V., Désert J.-M., Todorov K. O., Bean J. L., Stevenson K. B., Huitson C. M., Fortney J. J., Bergmann M., 2022a, MNRAS, 510, 3236

Panwar V., Désert J.-M., Todorov K. O., Bean J. L., Stevenson K. B., Huitson C. M., Fortney J. J., Bergmann M., 2022b, MNRAS, 515, 5018

Parker L. T. et al., 2024, preprint (arXiv:2405.08867)

Pecaut M. J., Mamajek E. E., 2013, ApJS, 208, 9

Pedregosa F. et al., 2011, J. Mach. Learn. Res., 12, 2825

Petrus S. et al., 2024, ApJ, 966, L11

Phillips M. W., Liu M. C., Zhang Z., 2024, ApJ, 961, 210

Pinna E. et al., 2016, in Marchetti E., Close L. M., Véran J.-P., eds, Proc. SPIE Conf. Ser. Vol. 9909, Adaptive Optics Systems V. SPIE, Bellingham, p. 99093V

Pinna E. et al., 2021, preprint (arXiv:2101.07091)

Plummer M. K., Wang J., Artigau É., Doyon R., Suárez G., 2024, preprint (arXiv:2403.04840)

Pont F., Zucker S., Queloz D., 2006, MNRAS, 373, 231

Popinchalk M., Faherty J. K., Kiman R., Gagné J., Curtis J. L., Angus R., Cruz K. L., Rice E. L., 2021, ApJ, 916, 77

Por E. H., Haffert S. Y., Radhakrishnan V. M., Doelman D. S., van Kooten M., Bos S. P., 2018, in Close L. M., Schreiber L., Schmidt D., eds, Proc. SPIE Conf. Ser. Vol. 10703, Adaptive Optics Systems VI. SPIE, Bellingham, p. 1070342

Radigan J., Jayawardhana R., Lafrenière D., Artigau É., Marley M., Saumon D., 2012, ApJ, 750, 105

Radigan J., Lafrenière D., Jayawardhana R., Artigau E., 2014, ApJ, 793, 75

Reback J. et al., 2022, pandas-dev/pandas: Pandas 1.4.2. Zenodo (online)

Rickman E. L., Ségransan D., Hagelberg J., Beuzit J. L., Cheetham A., Delisle J. B., Forveille T., Udry S., 2020, A&A, 635, A203

Rickman E. L. et al., 2022, A&A, 668, A140
Rickman E. L. et al., 2024, A&A, 684, A88
Rigby J. et al., 2023, PASP, 135, 048001
Röser S., Schilbach E., 2020, A&A, 638, A9
Ruane G. et al., 2018, in Lystrup M., MacEwen H. A., Fazio G. G., Batalha N., Siegler N., Tong E. C., eds, Proc. SPIE Conf. Ser. Vol. 10698, Space Telescopes and Instrumentation 2018: Optical, Infrared, and Millimeter Wave. SPIE, Bellingham, p. 106982S
Scargle J. D., 1982, ApJ, 263, 835
Schwarz H., Ginski C., de Kok R. J., Snellen I. A. G., Brogi M., Birkby J. L., 2016, A&A, 593, A74
Seabold S., Perktold J., 2010, in 9th Python in Science Conference. SciPy, Austin, Texas
Siess L., Dufour E., Forestini M., 2000, A&A, 358, 593
Skemer A. J. et al., 2015, in Shaklan S., ed., Proc. SPIE Conf. Ser. Vol. 9605, Techniques and Instrumentation for Detection of Exoplanets VII. SPIE, Bellingham, p. 96051D
Skemer A. J. et al., 2016, ApJ, 826, L17
Skemer A. J., Hinz P., Stone J., Skrutskie M., Woodward C. E., Leisenring J., Briesemeister Z., 2018, in Evans C. J., Simard L., Takami H., eds, Proc. SPIE Conf. Ser. Vol. 10702, Ground-based and Airborne Instrumentation for Astronomy VII. SPIE, Bellingham, p. 107020C
Skrutskie M. F. et al., 2006, AJ, 131, 1163
Skrutskie M. F. et al., 2010, in McLean I. S., Ramsay S. K., Takami H., eds, Proc. SPIE Conf. Ser. Vol. 7735, Ground-based and Airborne Instrumentation for Astronomy III. SPIE, Bellingham, p. 77353H
Snellen I. A. G., Brandl B. R., de Kok R. J., Brogi M., Birkby J., Schwarz H., 2014, Nature, 509, 63
Snik F., Otten G., Kenworthy M., Miskiewicz M., Escuti M., Packham C., Codona J., 2012, in Navarro R., Cunningham C. R., Prieto E., eds, Proc. SPIE Conf. Ser. Vol. 8450, Modern Technologies in Space- and Ground-based Telescopes and Instrumentation II. SPIE, Bellingham, p. 84500M
Spiegel D. S., Burrows A., Milsom J. A., 2011, ApJ, 727, 57
Stolker T., Bonse M. J., Quanz S. P., Amara A., Cugno G., Bohn A. J., Boehle A., 2019, A&A, 621, A59
Stone J. M. et al., 2016, ApJ, 829, 39
Stone J. M., Skemer A. J., Hinz P., Briesemeister Z., Barman T., Woodward C. E., Skrutskie M., Leisenring J., 2018, in Evans C. J., Simard L., Takami H., eds, Proc. SPIE Conf. Ser. Vol. 10702, Ground-based and Airborne Instrumentation for Astronomy VII. SPIE, Bellingham, p. 107023F
Stone J. M. et al., 2020, AJ, 160, 262
Stone J. M. et al., 2022, in Evans C. J., Bryant J. J., Motohara K., eds, Proc. SPIE Conf. Ser. Vol. 12184, Ground-based and Airborne Instrumentation for Astronomy IX. SPIE, Bellingham, p. 1218442
Strassmeier K. G. et al., 2015, Astron. Nachr., 336, 324
Strassmeier K. G., Ilyin I., Steffen M., 2018a, A&A, 612, A44
Strassmeier K. G., Ilyin I., Weber M., 2018b, A&A, 612, A45
Strassmeier K. G. et al., 2018c, in Evans C. J., Simard L., Takami H., eds, Proc. SPIE Conf. Ser. Vol. 10702, Ground-based and Airborne Instrumentation for Astronomy VII. SPIE, Bellingham, p. 1070212
Su K. Y. L. et al., 2006, ApJ, 653, 675
Sutlieff B. J. et al., 2021, MNRAS, 506, 3224
Sutlieff B. J. et al., 2023, MNRAS, 520, 4235
Tackett S., Herbst W., Williams E., 2003, AJ, 126, 348
Tan X., Showman A. P., 2019, ApJ, 874, 111
Tan X., Showman A. P., 2021, MNRAS, 502, 678
Todorov K. O. et al., 2019, A&A, 631, A169
Tofflemire B. M., Wisniewski J. P., Kowalski A. F., Schmidt S. J., Kundurthy P., Hilton E. J., Holtzman J. A., Hawley S. L., 2012, AJ, 143, 12
van Sluijs L. et al., 2023, MNRAS, 522, 2145
Virtanen P. et al., 2020, Nat. Methods, 17, 261
Vos J. M. et al., 2019, MNRAS, 483, 480
Vos J. M., Faherty J. K., Gagné J., Marley M., Metchev S., Gizis J., Rice E. L., Cruz K., 2022, ApJ, 924, 68
Vos J. M. et al., 2023, ApJ, 944, 138
van der Walt S. et al., 2014, PeerJ, 2, e453
Wang J. J. et al., 2014, in Ramsay S. K., McLean I. S., Takami H., eds, Proc. SPIE Conf. Ser. Vol. 9147, Ground-based and Airborne Instrumentation for Astronomy V. SPIE, Bellingham, p. 914755
Wang J. J., Kulikauskas M., Blunt S., 2021a, whereistheplanet: Predicting positions of directly imaged companions, Astrophysics Source Code Library, record ascl:2101.003
Wang J. J. et al., 2021b, AJ, 162, 148
Wang J. J. et al., 2022, AJ, 164, 143
Ward-Duong K. et al., 2021, AJ, 161, 5
Wenger M. et al., 2000, A&AS, 143, 9
Whiteford N. et al., 2023, MNRAS, 525, 1375
Wilson J. C. et al., 2008, in Schöller M., Danchi W. C., Delplancke F., eds, Proc. SPIE Conf. Ser. Vol. 7013, Optical and Infrared Interferometry. SPIE, Bellingham, p. 70133A
Wright E. L. et al., 2010, AJ, 140, 1868
Xuan J. W. et al., 2022, ApJ, 937, 54
Yang H. et al., 2016, ApJ, 826, 8
Zhou Y., Apai D., Schneider G. H., Marley M. S., Showman A. P., 2016, ApJ, 818, 176
Zhou Y., Bowler B. P., Morley C. V., Apai D., Kataria T., Bryan M. L., Benneke B., 2020, AJ, 160, 77
Zhou Y., Bowler B. P., Apai D., Kataria T., Morley C. V., Bryan M. L., Skemer A. J., Benneke B., 2022, AJ, 164, 239

This paper has been typeset from a TEX/LATEX file prepared by the author.